Controlling magnetic phases in SrMnO$_3$ through strain and oxygen annealing pressure

Author:
S. Schilstra

Supervisor:
prof. dr. T. Banerjee
Referent:
prof. dr. ir. B.J. Kooi

Daily supervisor
J.J.L. van Rijn

July 5, 2022

Abstract

Antiferromagnets retain a zero net magnetization when removed from an external magnetic field. These materials are highly interesting for high density data storage and, if also exhibiting ferroelectric properties, new transistor technology known as magnetoelectric spin orbit circuits [1]. Still, little effort has been done to accurately describe the magnetic order of a multitude of interesting materials. This thesis explores complex oxides, a material group that can exhibit antiferromagnetism and ferroelectricity. These materials are highly tunable with account to charge, spin, lattice and orbital and all these properties influence one another. The aim is to exploit this coupling by varying strains at the interface with different substrates. Distinct phases of both ferromagnetic and antiferromagnetic ordering are created with these strains. It is known that the magnetic order in complex oxides is altered when oxygen vacancies are present [2]. A method of high oxygen annealing after deposition is explored here. Epitaxial thin films of $SrMnO_3$ where grown using Pulsed Laser Deposition(PLD). Reflection High-Energy Electron Diffraction(RHEED) images suggests 2D growth and the AFM concludes the surface has low roughness. RHEED and X-Ray Reflection(XRR) both confirm a film thickness of 12 nm. The X-Ray Diffraction(XRD), Reciprocal Space Map(RSM) and Atomic Force Microscopy(AFM) reveal that an oxygen annealing pressure of 1 bar leads to an non-epitaxial phase of $SrMnO_3$ when grown on a $DyScO_3$ substrate, While $SrMnO_3$ grown on $SrTiO_3$ strains in a similar manner when annealed at 100 mbar or 1 bar. Magnetization studies suggest that the increased oxygen annealing pressure has lead to less oxygen vacancies for the $SrMnO_3$ on $SrTiO_3$ film but further studies need to be conducted.

Contents

Chapter 1

Introduction

Due to limitations in our current technology we need to improve computer storage and computing mechanisms even if this means adopting new types of devices. One promising example of this are magnetoelectric spin orbit circuits which could be an alternative to our current transistor technology [1]. These devices need materials that exhibit certain qualities, one of these qualities is multiferroicity which means that the material shows magnetic as well as electrical ordering. These two ordering can also be coupled. Antiferromagnetic ordering could be even better due to their high magnon velocity and minimal interaction between closely spaced antiferromagnets. A material group that can show this are metal oxides with a perovskite crystal structure. The most interesting characteristic of these materials is that they are strongly correlated electron systems meaning that altering some aspect of the material where electrons are involved can radically change all the other properties. This coupling is shown in figure 1.2 . Materials can for instance change there magnetic or electrical properties because of straining. A material that is a part of this group of versatile materials is $SrMnO_3$ (SMO), which is the focus of research in this thesis. Straining the material is done by depositing it on substrates that have larger lattice parameters, the materials that where used as substrates in this research are $DyScO_3$(DSO) and $SrTiO_3$(STO) with lattice parameters visible in figure 1.1. The focus on this thesis will lay on controlling the magnetic order by modulating the oxygen concentration contained in the crystal. The modulation of oxygen is done during one aspect of deposition, annealing. Annealing is the heating of the film to allow it to rearrange itself such that the number of dislocations decrease. The film is exposed to high temperature for a set amount of time and subsequently slowly cooled down to room temperature. The parameter fluctuated in the experiment is the oxygen pressure whilst annealing. This parameter is interesting because oxygen vacancies in the metal oxides can change the material properties, which include the magnetic properties. It is hypothesized that high oxygen pressure will yield less oxygen vacancies in the material. These oxygen vacancies can impose many effects on the materials such as allowing the material to be an electrical conductor (section 2.2). If the perovskite contains oxygen vacancies it will also distort its crystal structure and since the crystal structure of the perovskite is of importance for almost all of the material properties the material could function entirely different compared to the same material without oxygen vacancies. Thus an abundance of different material phases can be found, this research will confine itself mostly to the differences in magnetic properties due to high and low oxygen pressure annealing. SMO can theoretically show multiferroicity when strained as seen in figure 2.5, however oxygen vacancies can hinder the formation of the wanted antiferromagnetic phase. This research controls these vacancies by altering the oxygen annealing pressure and verifies this control by magnetic measurements. This research involves DSO and STO substrates that will have SMO thin films deposited on top. Both substrates will have an SMO film grown with a high annealing pressure of 1 bar and a low annealing pressure of 100 mbar. To prove that the increased pressure lowered the amount of oxygen vacancies the magnetic properties where determined with a Magnetic Properties measurement System(MPMS). The SMO was grown on the substrate using Pulsed Laser Deposition(PLD). During deposition the amount of layers of SMO deposited on the substrates was monitored using a Reflection High-Energy Electron Diffraction(RHEED) system. Analysis of the surface of the films was done utilising Atomic Force Microscopy(AFM). An inspection of the structure of the film was done with X-Ray Diffraction(XRD).
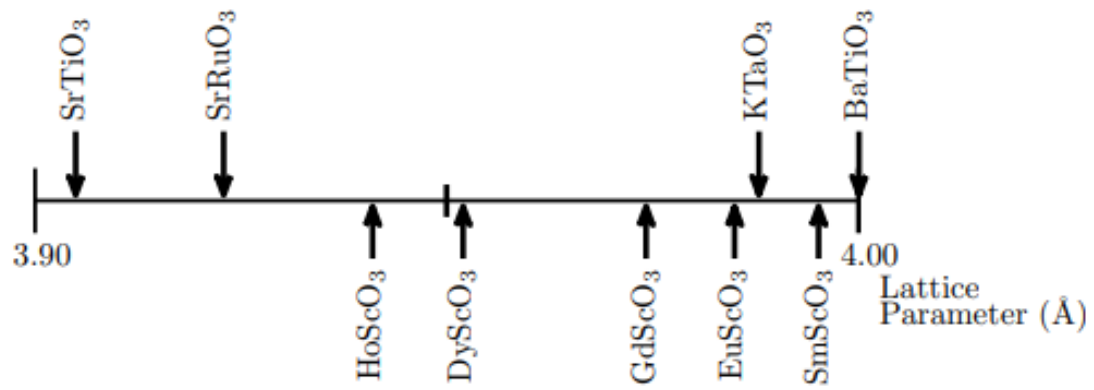
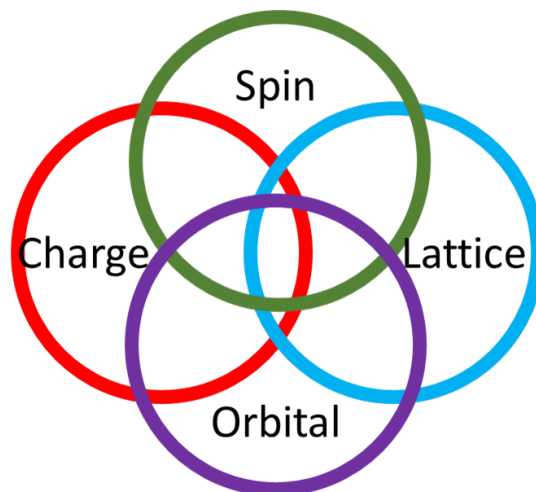Figure 1.1: The crystal lattice parameter of a multitude of complex oxides [3]

Figure 1.2: Strongly correlated electron systems couple these four parameters

Chapter 2

Theory

2.1 Magnetism

Magnetism is the attraction or repulsion of materials or systems due to a magnetic field. Magnetic fields can be generated by electric currents and the inherent magnetic moment of elementary particles. All materials are generally one of these four types of magnets; ferromagnet, antiferromagnet, diamagnet and paramagnet.

2.1.1 Ferromagnetism

In day to day life ferromagnets are called magnets because these materials show the strongest magnetisation, which is the sum of the magnetic moments within a magnetic volume. Ferromagnets will retain their magnetisation when they are no longer exposed to an external magnetic field, this is called spontaneous magnetization. In ferromagnetic material neighbouring magnetic moments are coupled due to an exchange interaction such that neighbouring atoms have the same magnetic moment direction. One could now think that every ferromagnetic moment in the entire material will point in the same direction but this is not the case. Domains with a certain magnetic orientation form in ferromagnetic materials. These domains form because if all magnetic moments are aligned this will give rise to a large magnetic field outside of the material which will require a lot of energy. Domains lower this energy by orientating such that some or all of the magnetic moments cancel each other out. Between these domains domain walls are formed. There are different energies to consider when understanding how the domains and the domain walls are formed such as anisotropy and exchange energy but the details will not be disclosed here.

The property of ferromagnets to retain their magnetization while no external field is present is called hysteresis. If an increasing magnetic field is applied in one direction to a ferromagnet, the magnetization will increase until a maximum is reached, this maximum magnetization is called the saturation magnetization (M_s) and the field to reach this maximum is the saturation field (H_s). After reaching saturation and removing the external magnetic field the ferromagnet will be left with some remnant magnetization(M_r). An increasing magnetic field can be applied in the opposite direction to eventually remove the magnetisation from the ferromagnet. The field needed for this is called the coercive field (H_c). The field could be increased further to reach M_s again but this time it will be negative because the anti parallel direction. The previous steps can be repeated by switching the field direction again to return to the original M_s where M_r and H_s will also be determined again but negatively. This process can graphically be shown in a magnetisation-applied field(M-H) graph. The M-H graph of a ferromagnet shows a loop due to hysteresis and is called the hysteresis loop which is the most characteristic and interesting feature of ferromagnets. From this loop, ferromagnetic properties such as magnetic anisotropy and softness can be studied. Magnetic anisotropy describes how magnetic properties can differ for an object depending on direction. Softness of a magnet is a quality linked to the H_C of a magnet, where a soft magnet is easy to magnetize and thus has a low H_C. Another important value for ferromagnets is the Curie temperature. If a ferrromagnet's temperature rises it will slowly lose it's magnetization until it is completely gone, this is the Curie temperature. At the Curie temperature the magnet will lose its ferromagnetic properties because the magnetic moments will no longer be coupled due to the high thermal energy. This causes the ferromagnet to behave like a paramagnet which will be discussed

later. Since normally ferromagnets retain magnetization, heating the magnet above Curie temperature can be used to clear the magnetization. When the material is now cooled below Curie temperature the material will acquire a small amount of magnetization. This is the case because the magnet will order itself again below Curie temperature. While the ordering is mostly random the anisotropy of the material still often leads to some non-zero magnetization [4].
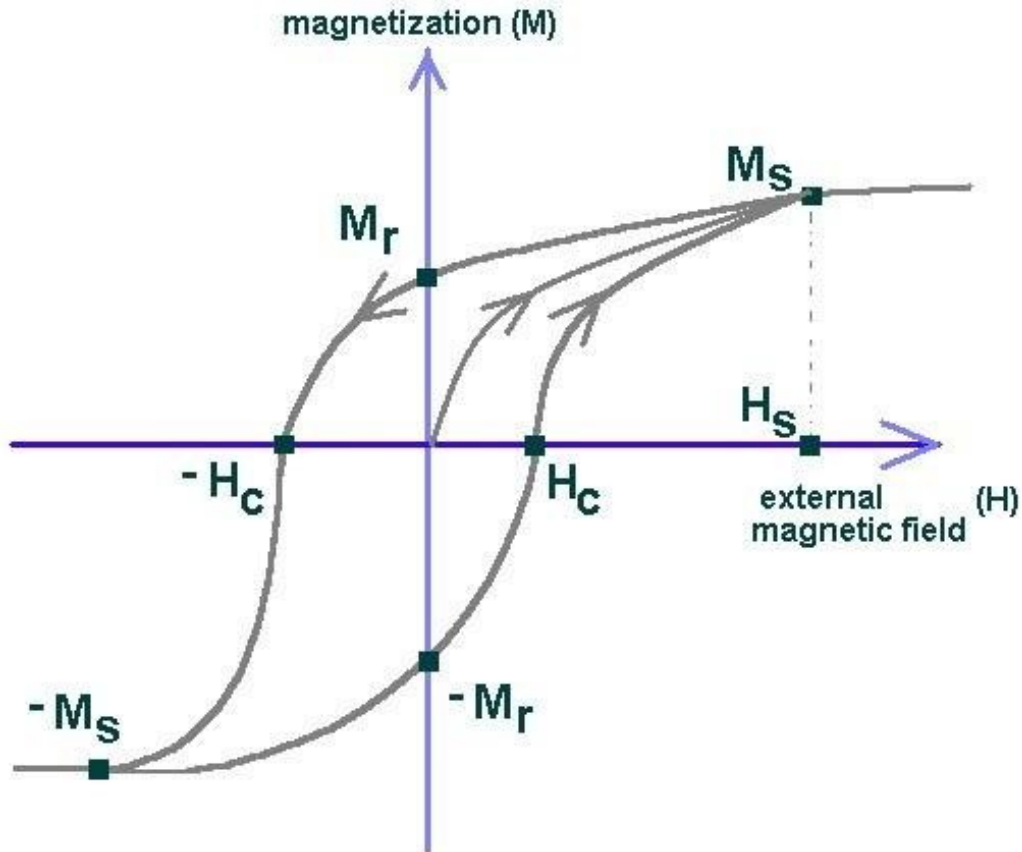

Figure 2.1: A general ferromagnetic M-H graph [5]

2.1.2 Antiferromagnetism

Antiferromagnets are similar to ferromagnets except the magnetic moments are coupled in a way that causes them to be in anti parallel order. This leads to the material not having magnetization. There are many different ways to have antiferromagnetic coupling in a crystal lattice and these are called antiferromagnetic types. The different types are denoted by a letter and reveal how the magnetic moment of the nearest neighbour atoms will be oriented as seen in figure 2.2. Measuring antiferromagnets is challenging because they do not show a net-magnetization (or a really small one) and distinguishing the antiferromagnetic types from one another is also a challenge because this has to be done by probing the magnetic moment of the nearest neighbours. This weak magnetization is what makes antiferromagnetic data storage appealing since the memory elements will not interact with one another allowing for a high density of memory elements. This is a property that ferromagnets do not share because their bigger magnetization means they might influence each other. Furthermore the spin dynamics of a antiferromagnet lie in the THz range while for ferromagnets this lies in the GHz range, significantly slower. This could be possible reasons for choosing antiferromagnetic computer memory. Antiferromagnets also have a critical temperature

beyond which the material is no longer antiferromagnetic. In the case of antiferromagnets this is the Néel temperature. It will behave like a paramagnet above it until cooled below Néel temperature again similar to the ferromagnet [4].
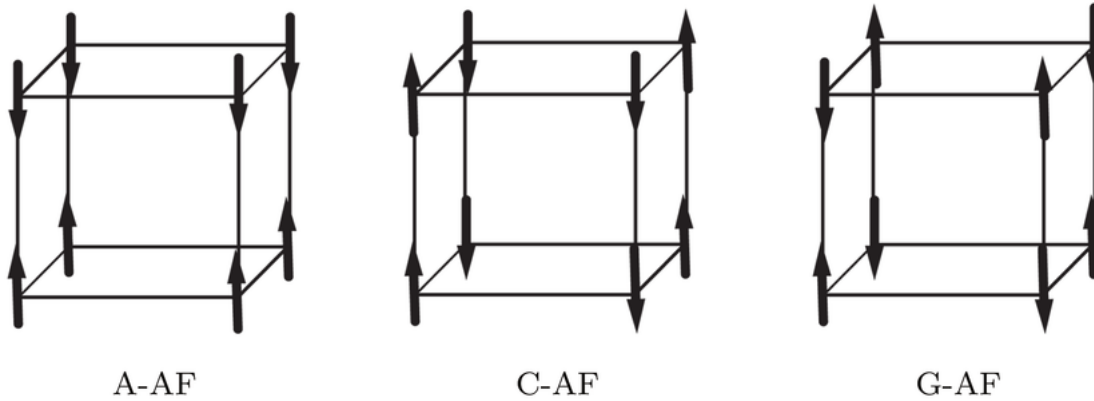

Figure 2.2: A representation of possible antiferromagnetic ordering [6]

2.1.3 Paramagnetism

Paramagnets are weakly attracted to an applied magnetic field and lose their magnetization as the applied field reaches zero. Their Magnetic susceptibility is about 10^-6 to 10^-8 as small as ferromagnets leading to this weak magnetization. Paramagnetism is caused by unpaired electrons, these electrons have a magnetic moment that will align with the applied field. Since there is no coupling between the atoms that will align the magnetic moments it does not share many of the qualities of ferromagnets, only the magnetization direction is the same. The magnetization of this magnetic type is linear with the applied magnetic field [4].

2.1.4 Diamagnetism

Diamagnets will weakly oppose an applied magnetic field and do not retain their magnetization in the absence of a field. Their Magnetic susceptibility is two orders of magnitude lower than paramagnets and in the other direction. Diamagnets can be explained by electrons creating current loops in the their orbitals to oppose the magnetic field. All materials are Diamagnetic but because this effect is so small other magnetic types often dominate the magnetization. If there is no other magnetic contribution a large magnetic field or precise measurement devices can be utilised to observe it. The magnetization has a linear relation with the applied field [4].
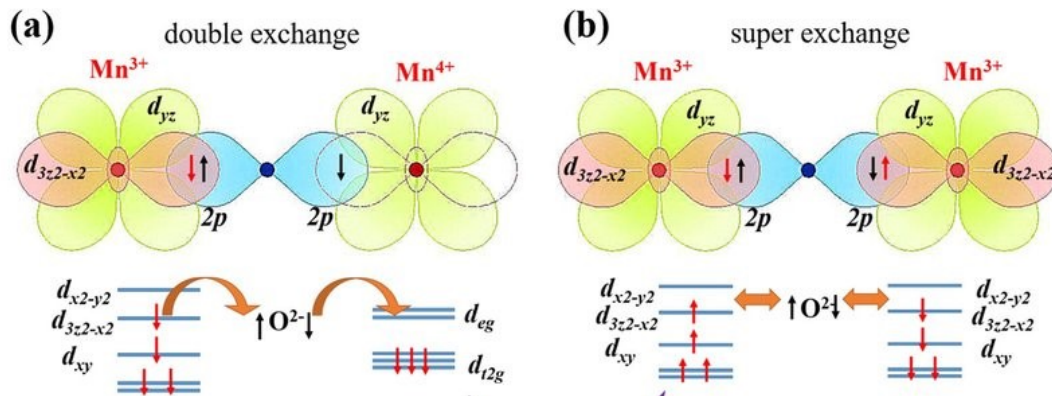
2.2 Exchange interactions

Figure 2.3: Double and Superexchange [7]

2.2.1 Double exchange

Double exchange is an effect that causes a material to be ferromagnetic and enables electric conduction. The effect arises in materials that have at least two types of cations with a valency difference of one. The material should also contain an anion. The anion can give one of its electrons to the lower valency cation. This leaves a vacancy in the anion which the higher valency cation can fill up by giving up one of its electrons. After this process the high valency cation has become the low valency cation, just as the low valency cation becomes the high valency cation. This process has now returned the system to the original state but the valencies of the cation are swapped thus these states are degenerate as can also be seen in figure 2.3. This allows this process to continue indefinitely and is called hopping. The ability to hop lowers the kinetic energy.

The reason this leads to ferromagnetism is that the anion supplies a spin, say spin up, then the spin up electron from the anion can easily hop in the cation's orbital if the outer shell of the cation is at least half filled with spin down, allowing only spin up to enter the orbital because of Pauli's exclusion principle or if it is less than half filled with spin up electrons, where Hund's rule allows the spin up electron to sit in the orbital. Now the other cation can fill the vacancy in the anion again while not having to undergo any spin flipping if this cation has the same spin as the other. The spins thus all have to be up because if the anion gives a spin up electron it can only be filled back up by a spin up electron because spin conservation does not allow the spin to flip.

This causes the magnetic moment of the spin to all point in the same direction leading to ferromagnetism. How much every atom contributes to the magnetization is dependent on the amount of unpaired electrons it has, a higher amount of unpaired electrons means more magnetic moment in one direction. Paired electrons do not contribute because they have opposite spin and cancel each others magnetic moment.

When we broaden our view to not just 2 cation but a long line of alternating valency cations with anions in between, the electron could hop along the entire line allowing for conduction. In a crystal with a lot of these double exchange sites the electrons can move through the material and will thus be conducting.

2.2.2 Superexchange

Superexchange is an effect that causes materials to be antiferromagnetic. This effect arises between two next-to-nearest cations facilitated by an anion. The cations should have the same valency for this effect to be present. If one where to look at the allowed excited states in the case of parallel or anti-parallel unpaired electron spins of one cation with respect to the other, the anti-parallel coordination has more of these allowed excited states. This is the case because the up and the down spin electrons of anion can both enter one of the cations without undergoing a forbidden spin-flip. Which means that the anti-parallel coordination is lower in energy and this will be the

spin configuration the system will be in. This anti-parallel spin will lead to the material being antiferromagnetic as can be seen in figure 2.3. This effect does not facilitate electrical conduction because these other possible states are excited states and not a different ground state as is the case with double exchange.

2.3   Crystal structure

The perovskite crystal structure is a three dimensional crystal structure following the chemical formula ABX_3 involving two types of cations usually one larger, "A" than the other, "B" and a type of anion, "X" which will often be oxygen. The crystal unit cell consists of a cube with "B" in the middle and "A" at the corners of the cube. The "B" is encapsulated by an octahedron of "X" these atoms will lay in the middle of the faces of the cube as seen in figure 2.4. This will give rise to the ideal cubic perovskite structure, however this is not the structure often encountered. The perovskite will often show some sort of deformation. The perovskite could be tetragonal or orthorhombic, stretching the cube such that not all the sides are one length "a" but two or all three sides are a different length respectively. It could also be that the octahedra are slightly tilted. If one octahedra tilts others in the crystal will also tilt and this could destroy symmetries and change positions of not only the X atoms but the others too [8]. The electric polarization of the perovskite material is determined by the structure. The electric polarization gets generated by an off-centered "B" cation. The side the "B" is closer to becomes more positively charged and the opposite side more negatively charged. This will lead to an electric field forming. The "B" cation could move off-center due to the structure being tetragonal because this will cause the "X" octahedron to compress along 2 directions and push the "B" out of the middle. Multiple energy contributions will decide how and if this will show in the material [9].

In the process of making thin films of perovskite material it could happen that the perovskite does not form entirely as expected. The perovskite could have some structural defects. One type of defect that is known to happen and can yield a large impact on the material are oxygen vacancies. These make it such that the perovskite is formed with an oxygen atom less than normal [2]. The perovskite still has to be neutral and thus some of the "B" cation become less positive to compensate. The presence of less positive cations in the compound induces a mixed valency which in turn promotes double exchange as explained in section 2.2.1.

The structure with its small defects can often lead to anisotropy in the complex oxides. This leads to the material properties varying depending on the direction they are measured in.
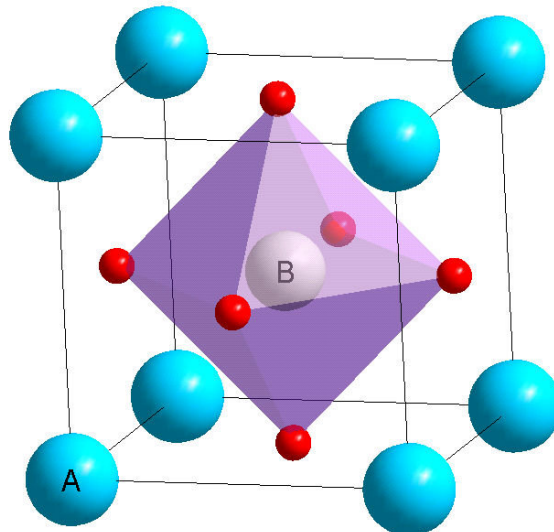

Figure 2.4: Unit cell of the perovskite crystal structure [10]

2.4 Materials

2.4.1 SrMnO$_3$

SrMnO$_3$(SMO) is a material that is hexagonal crystal structure at room temperature and below but can adopt a perovskite structure when deposited on top of a matching cubic surface, such as another perovskite. This material is insulating and antiferromagnetic due to the high amount of superexchange. SrMnO$_3$ is the material grown on the substrates. The Mn^{4+} - O^{2-} - Mn^{4+} bond makes it such that SMO inhibits superexchange. This leads to SMO being an antiferromagnetic material if there are no defects. When oxygen vacancies are introduced however, this material can exhibit ferromagnetism. The oxygen vacancies allow Mn^{3+} into the crystal to ensure neutrality of the material. This will allow Mn^{4+} - O^{2-} - Mn^{3+} bonds to form which will give rise to double exchange and consequently ferromagnetism. The lattice parameter of SMO is 3.805Å [11]

2.4.1.1 Strain Dependence

This material is known to be very versatile in the sense of it having many different electric and magnetic phases. This difference in phases is mostly due to how much the perovskite is strained and the temperature. Strain is calculated with this simple formula

$$\epsilon = \frac{A_s - A_0}{A_0}$$

Where ϵ is the strain,
A_0 is the lattice parameter in bulk(unstrained),
A_s is the lattice parameter when strained

Using a first-principles-based model different possible phases have been determined and are shown in figure 2.5. The figure shows antiferromagnetic phases G, C and A that are visible in figure 2.2 and paramagnetic phases(PM). The ferroelectric(FE) and paraelectric(PE) phases are also shown. The main interesting phase is the yellow antiferromagnetic and ferroelectric phase. This is because it is multiferoic even at room temperature. The multiferoicity is important because this is the material property that is interesting for new technologies like magnetoelectric spin orbit circuits. If this multiferoicity is present above room temperature the device would not have to be cooled which of course simplifies the potential devices that could be fabricated and saves energy.

While figure 2.5 is one prediction of the possible phases there has also be suggested by other models that their could also be ferromagnetic states when SrMnO$_3$ is strained to around 0.03 [12].
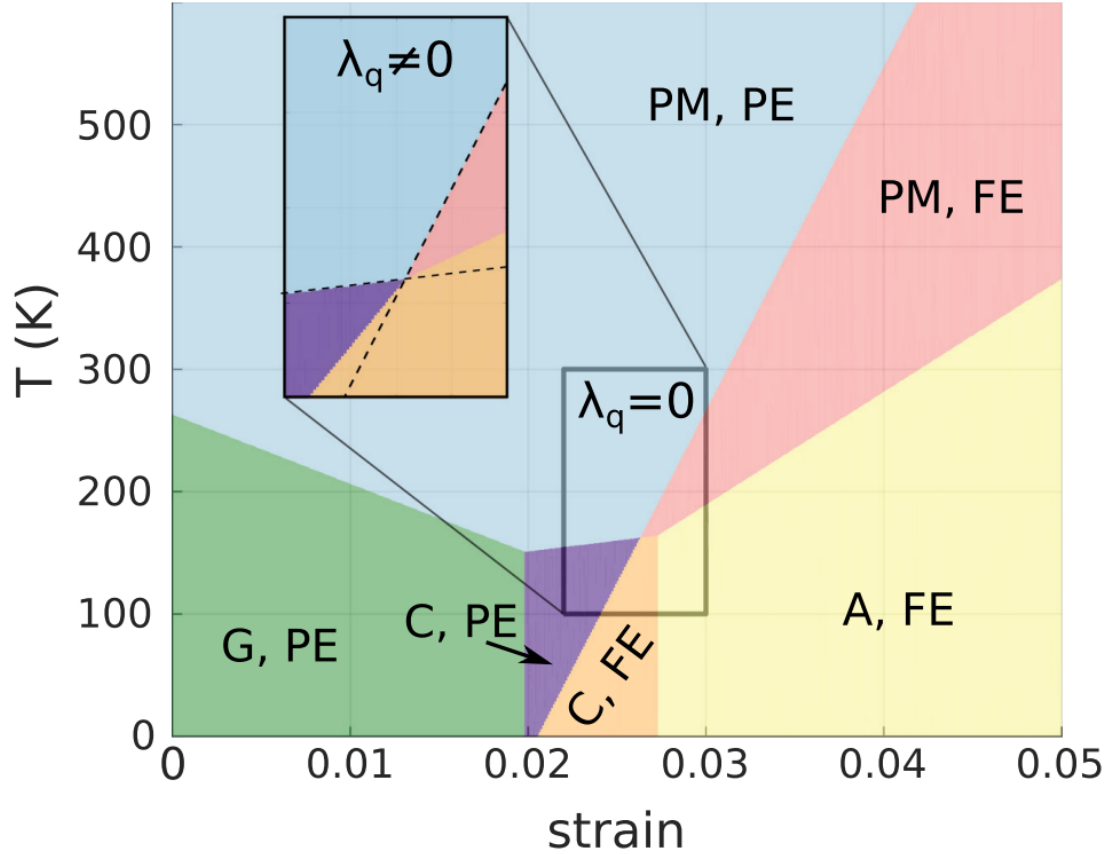
Figure 2.5: Theoretical magnetic and electric phases of $SrMnO_3$ due to in-plane strain and temperature [13]

2.4.2   DyScO$_3$

$DyScO_3$ is also a complex oxide with the perovskite crystal structure. It is a paramagnetic material. This is one of the materials that will be used as a substrate to strain the $SrMnO_3$. $DyScO_3$ does not have a regular perovskite crystal structure. The Dy atoms are surrounded by eighth distorted Sc-O octahedra. It has a orthorombic crystal structure and hence has varying a, b and c lattice parameters. This is different from the regular perovskite structure that has the same lattice parameter along all sides.The material can however be described as a pseudo-cubic perovskite but the crystal orientation will differ between the two crystal structures. The substrates used had a (110) orientation for their actual crystal which this leads to a pseudo-cubic orientation of (001). The lattice parameter of the pseudo-cubic unit cell is 3.949 Å [14]. The strain induced by DSO on the SMO film can be found in table 2.1

2.4.3   SrTiO$_3$

$SrTiO_3$ is a complex oxide with a cubic perovskite crystal structure. This material is diamagnetic. This material will be used as a substrate oriented in the (001) direction. This material has a lattice parameter of 3.905 Å [11]. The strain induced by STO on the SMO film can be found in table 2.1. The substrate where the thin films are grown on have a certain crystal orientation given by Miller indices as seen in both the STO and SMO sections. This orientation is however not exactly correct. The angle of this orientation is always slightly off from the exact crystal orientation. This angle is called the miscut angle and this angle will lead to structures on the surface of the substrate. The structures are called terraces. Terraces form because the miscut makes it so that one uninterrupted sheet of crystals is not the most flat way to arrange the top of the substrate. Instead the surface of the substrate will show a step like structure where the steps height is a single unit cell and the step length is large amount of unit cells dependent on the miscut angle. We will see that this effect is especially prevalent on the STO films.

substrate	A(in-plane) (Å)	ϵ(in-plane) (%)	C(out-of-plane) (Å)	ϵ(out-of-plane) (%)
STO	3.905	2.63	3.756	-1.29
DSO	3.949	3.78	3.743	-1.63

Table 2.1: Experimentally found SMO strain and lattice parameter due to STO and DSO when the SMO is fully strained [11]

2.5   Diffraction

Diffraction is an effect where a wave encounters an object or opening and causes the wave to behave in certain ways. This could be X-rays for instance that diffract of a grating. In the context of this thesis there are two important concepts, these are the Bragg's law and reciprocal space. Bragg's law is an expression that shows how a crystal structure will diffract waves. The waves will diffract of a crystal plane, a plane of atoms in the crystal. Waves will give positive interference when there is an integer amount of wavelengths in path length difference between the two waves. This is observed in the expression here

$$n\lambda = 2d\sin\theta$$

Where n is an integer amount of wavelengths,
λ is the wavelength of the wave,
d is the spacing between crystal planes,
θ is the angle between the waves and the crystal plane.

When studying crystal structures a concept known as the reciprocal lattice can be of great help. The reciprocal lattice is a Fourier transform of the regular crystal lattice, the direct lattice. The reciprocal lattice is a lattice consisting of points. These points signify a certain spatial frequency. A point appearing on the reciprocal lattice means that the direct lattice has a certain periodicity and thus this can be used to determine the distance between crystal planes. Diffraction can preform this Fourier transform for us and allow us to observe the reciprocal lattice.

Chapter 3

Experimental methods

3.1 Fabrication techniques

The STO and DSO substrates are acquired and subsequently SMO is deposited on top. The techniques of this deposition are explained here.

3.1.1 Pulsed Laser Deposition

Pulsed Laser Deposition is a technique where laser pulses hit a target material to deposit this material on to a substrate to create a thin film, a material layer with a magnitude in the order of nano to micro meters. This method of deposition is used because of the good control on the layer by layer growth and is known for fabricating thin films that are highly reproducible. PLD creates a plasma plume at the target by firing a high energy laser pulse at the surface. The laser beam penetrates the surface a few nano meters deep. The laser creates such a high electric field that electrons are removed from the atoms. These free electrons will oscillate due to the electromagnetic oscillations of the laser and if these high energy electrons collide with the atoms the material will be heated. This heat will case the target to emit a vapor cloud of the atoms and most of these have lost some electrons this leads to the vapor being a plasma vapor. PLD is conducted in a vacuum chamber to ensure the plasma reaches the substrate without being obstructed by background gasses and to limit the amount of contamination's in the thin film. The chamber can be filled with a gas as to possibly improve the thin film structure by creating bonds with the gas, the gas additionally allows the vapor plume to behave differently, impacting the deposition or "growth" of the thin film. The laser is in pulses because it will have to charge in between exposure because of the high energy and it will also allow the film to rearrange itself shortly. The substrate is constantly heated to assist rearranging and to decrease the nucleation density which will make it so the film is less likely to grow a rough surface with different islands of the target material. After the deposition is completed and the Film is grown to the desired thickness The sample is not yet removed. The film will now be annealed which means it will be maintained at a certain temperature and in our case some oxygen pressure is applied. This is done so the film can rearrange and to fill some portion of the oxygen vacancies. There are many tunable parameters involved with PLD, only looking at the laser's parameters there is the wavelength, pulse time, laser fluence, which is the energy per area. This will have to be taken into consideration when depositing.

3.1.2 Reflection High-Energy Electron Diffraction

Reflection High-Energy Electron Diffraction is a method to probe the amount of layers deposited during growth of a thin film. It utilises high energy electron beam at a shallow angle to the substrate and a detector screen at a shallow angle at the other side of the substrate. The electron beam diffracts of the thin film but only of the crystal planes close to the surface because the electrons can almost not penetrate through the films. This thus gives us a diffraction pattern highly dependent on the surface of the film and this gives some indication of the growth at that time. The RHEED pattern on the detector are bright diffraction peaks, the amount of visible peaks depends on the RHEED intensity and alignment. By monitoring the intensity of these spots we can determine if a new layer of material is completed. A certain oscillation in the intensity of the spots happen if the growth of the film is 2 dimensional layer-by-layer growth. This is caused

by a high amount of diffraction on completed crystal layers and a lower amount of diffraction on non completed layers. The surface of a completed layer will be flat and homogeneous and will thus allow for a high amount of diffraction. Before an entire new layer is grown the top surface will not be flat and have areas where the new layer is already present and areas where this is not the case. The waves will now have a harder time to diffract properly and the intensity of the diffraction spots will decrease a bit. A new peak will be found when the layer is completed again and so on. Exploiting these peaks we can determine, whilst growing, how many layers there have been deposited. Utilising knowledge of our materials crystal lattice we can determine the approximate thickness of the thin film at that point in time. The peaks allow us to correlate the amount of laser pulses to the amount of deposited material. This is important because the oscillations in intensity might not always be present due to the growth possible being less 2 dimensional or the grown thin film might interact with the electrons in a certain way to make the diffraction less dependant on the completeness of the layer. If these oscillations are lost at some point during deposition the amount of needed pulses to reach a certain thickness can be calculated and thus be used to obtain an approximate amount of layers and thickness. While this is the most important part, the shape of the diffraction spots and their position can also reveal something about surface level structures of the thin film. The diffraction spots lay on some circle if the film is mostly 2 dimensional, if the film grows more 3 dimensional, with islands, the diffraction spots will lay on a grid. [15] Kikuchi lines are another pattern that can be observed. They are lines where the diffraction spots lie in. They are formed due to inelastic scattered electrons and are associated with crystals that are low in defects. [16] The shape can change differently due to many different effects that will not be elaborated on.

3.2 Probing techniques

After the thin films are grown they are characterized. The methods used for probing the films are expanded upon here.

3.2.1 Atomic Force Microscopy

Atomic Force Microscopy is a surface topology probing method. It uses a small cantilever with a tip on the end to "feel" the surface topography by moving the sample along a plane. The cantilever will be affected by atomic forces when approaching the surface of the sample. The cantilever will first feel an attractive force when approaching, the Van der Waals force, followed by a repulsive force when getting even closer to the sample, the coulomb force, this repulsive force dominates when extremely close to the atoms. The tip of the cantilever gets pushed or pulled by these forces which leads to the cantilever being deflected. This deflection is used to determine the height of the coordinate the cantilever is at. The deflection is often determined by a laser reflecting of the top of the cantilever. AFM can be done in different modes, the main ones are contact or constant deflection, non-contact and tapping mode. Contact mode uses a constant deflection of the cantilever in the repulsive, close to surface, regime. The tip is almost dragged across the surface and the topography is determined by the control system of the cantilever that moves it up and down to maintain constant deflection. Since preforming AFM in atmospheric conditions causes surface moisture on the sample the tip has to be pressed in to the sample with great force to overcome the effects of the surface moisture. This high force combined with moving the tip to scan the surface can cause damage to both the tip and the sample. the second mode, non-contact mode, utilises the attractive regime slightly further from the surface of the sample. The tip is brought to near its resonance frequency. The amplitude and the resonance frequency of the cantilever changes due to the attractive forces. Either the frequency or the amplitude is maintained by feedback and this allows imaging of the surface. To secure that the tip does not get attracted too much and gets closer to the repulsive regime, a high spring constant is used in this mode. This high spring constant with the relatively weak Van der Waals force leads to a signal that is small and thus makes it difficult to map the topography accurately however because the low forces involved it is unlikely that this mode will damage the tip or surface. the third and most commonly used mode is the tapping mode. It is a combination of both the previous modes. The tip is again driven to oscillate near resonance but with a higher amplitude. Every oscillation will be in both the attractive and repulsive regime. The tapping will vary the amplitude, phase angle and resonance frequency. This technique is so often used because the forces are lower than contact mode since there is no constant pushing against the substrate, while giving a similar resolution to contact mode. [8]

3.2.1.1 Conductive Atomic Force Microscopy

Conductive Atomic Force Microscopy is an adaptation from regular AFM. The tip on the cantilever is conductive or coated with a conductive layer. The working principles are mostly the same besides that a potential difference is created between the tip and the plate the sample rests on, allowing c-AFM to examine conductive properties of the sample. If the sample does not conduct well conductive elements can be deposited on top of the sample and be brought into contact with the plate. This allows electricity to flow small distances which is useful for insulating materials and it also allows probing of a thin film even if the substrate is insulating. Since c-AFM allows probing of the topography whilst probing conduction a comparisons between possible domains and conduction can be made. While this is a powerful tool it should be noted that having a potential difference on the tip might cause attractive or repulsive effects due to the sample present which could distort the topological data. c-AFM can be used in most AFM modes although it is recommended to use it in modes that make close contact to the surface to allow for easier conduction. While c-AFM can be activated while doing a normal AFM scan, it can also do a voltage sweep at a specific point on the surface which allows for a more thorough examination of the behaviour of the sample at a specific point.

3.2.2 X-Ray Crystallography

X-Ray crystallography encompasses all techniques to probe a crystal structure with x-rays. Three techniques will be discussed here, X-Ray Reflection(XRR), X-Ray diffraction(XRD) and Reciprocal Space Map(RSM). XRR Reflects x-rays of thin films with a shallow angle and has a photo detector receive the signal at the same small angle. The signal received will depend on the reflection which is a result of Fresnel equations. When XRR is preformed on a thin film with at least two distinct material layers than reflection can happen of both layers. At some angels this can give constructive interference if the path length difference will be an integer amount of wavelengths. This will show as the signal undergoing some oscillations. The angular spacing between these oscillations reveal the thickness of the material on top. The XRR signal will also change according to the material densities and interface roughness although these effects are more subtle they are still important for the signal.

XRD uses diffraction to probe the lattice parameters. The set-up is the same as for XRR but the angle is larger. Something to note about the data of XRD and XRR is that 2θ is used instead of just θ this is because the detector is actually stationary and the laser rotates double the angle while the sample rotates by $\omega = 2\theta$. This is always the case for XRR but for XRD ω depends on what crystal plane peaks one seeks to probe, in case of $\omega = 2\theta$ it will be the out-of-plane peaks. The XRD signal will be comprised of large intensity peaks for the substrate's crystal planes because the substrate is a large part of the sample. These lattice parameters are known from literature and because the 2θ corresponds with a certain lattice parameter the system is aligned using these peaks. The deposited material will also show peaks although a bit smaller. These peaks will reveal if the material got strained by the mismatch in lattice parameter by comparing it to the lattice parameter of the bulk unstrained material. The peaks sometimes show fringes around the film peaks these indicate a crystalline growth of the film

RSM is a the same process as XRD. XRD is actually taking a line in reciprocal space and measuring the intensity over the line. RSM also does this but will do it for multiple lines next to each other mapping out an area in reciprocal space. So RSM is a collection of XRD signals. Taking a different line is done by altering the 2θ and ω relation. The RSM can also show if parts of the film are relaxed by noticing some slightly higher intensity trailing towards the bulk lattice parameters of the film.

3.2.3 Magnetic Properties Measurement System

The Magnetic Properties Measurement System uses a liquid Helium cooled Superconducting Quantum Interference Device(SQUID). This is a device that can measure changes of magnetic flux using superconductive coils. The magnetic sample is moved up and down to alter the magnetic flux and determine the magnetization of the sample. The MPMS is a very sensitive device and useful in measuring even magnetizations in the order of 10^{-8} emu. The system has options to fluctuate the temperature in a range of 5 K to 380 K. It can apply fields up to 7 T which are needed to ensure

magnetization of samples. The high fields are also used to linearly fit diamagnetic backgrounds in Magnetization - applied field graphs. and to subsequently subtract them from the magnetic data.

Chapter 4

Results and Discussion

A total of four samples where fabricated and are compared. Two DSO samples and two STO samples where created. The oxygen annealing pressure is the variable changed in the depositions. The aim is to find out if the films can be grown with a different oxygen pressure and if this allows us to control the oxygen vacancies in the material. The four distinct samples are shown in table 4.1

Substrates	Low oxygen (0.1 bar)	High oxygen (1 bar)
High strain (DSO)	DSO-L	DSO-H
Low strain (STO)	STO-L	STO-H

Table 4.1: All the fabricated and compared thin films

4.1   SrMnO$_3$ on DyScO$_3$

4.1.1   Growth characterization

Two types of SMO on DSO samples where created. The difference between them is the oxygen pressure during annealing post deposition. One of the samples, DSO-L, was exposed to a more regular 100 mbar of oxygen pressure during annealing while DSO-H was exposed to a higher 1 bar of oxygen pressure. Annealing was done at a temperature of 600°C for 1 hour. The temperature during deposition was 800 °C. The pulse frequency was 5 Hz. The oxygen pressure while depositing SMO was $5 \cdot 10^{-2}$ mbar. The pulsed laser used was a Krypton Fluoride laser with a wavelength of 248 nm. The fluence of the laser was 2 J/cm^2. The RHEED pattern was evaluated during deposition and extrapolated to determine the total number of laser pulses needed to grow SMO films of 30 unit cells and thus roughly 12 nm in height. The amount of laser pulses for DSO-L was 3650 and the amount of pulses for DSO-H was 3900. The samples where annealed before deposition at 960 °C with oxygen flow for 4 hours. The DSO substrate had a (110) orientation this would lead to a (001) pseudo-cubic orientation.

4.1.1.1   Reflection High-Energy Electron Diffraction
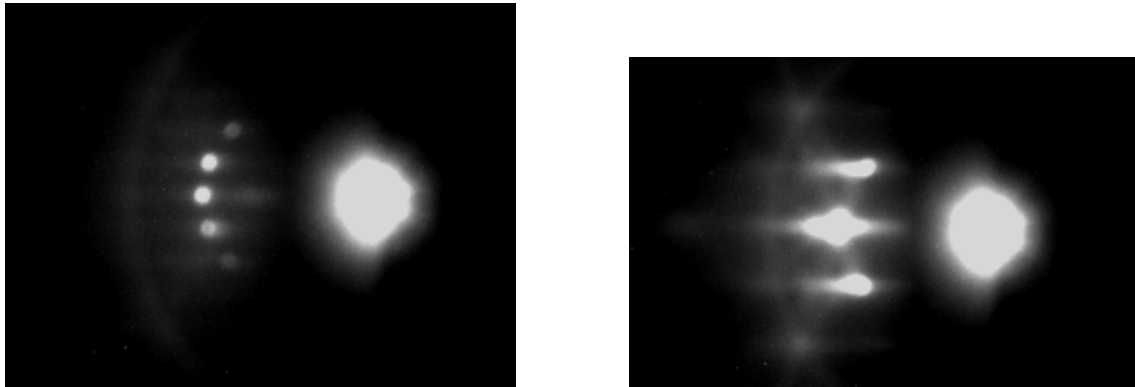
(a) Before
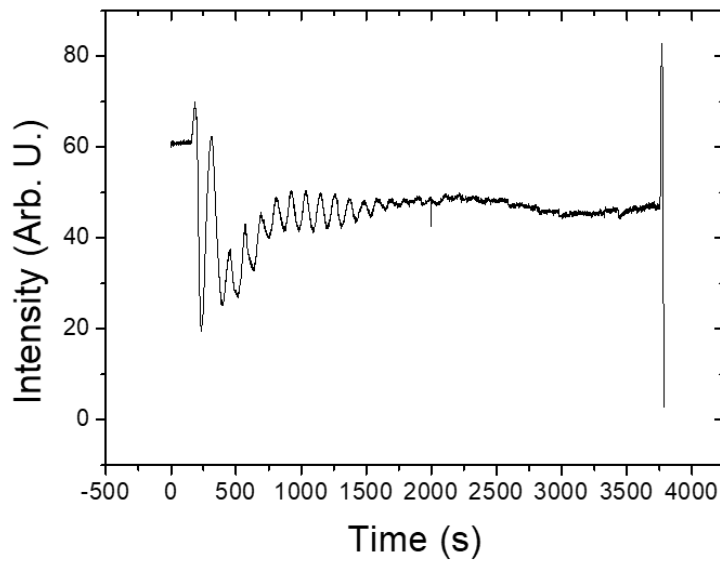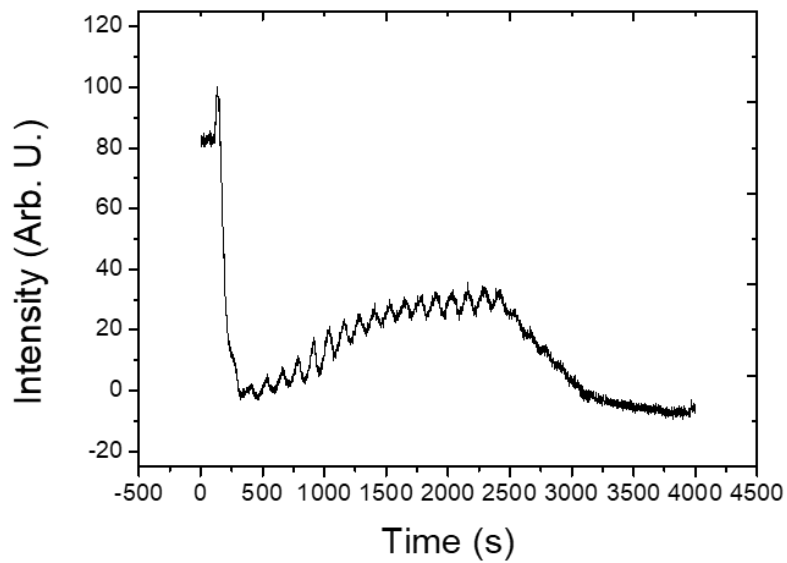

(b) After

(c) Diffraction spot intensity

Figure 4.1: RHEED of DSO-L, a) Diffraction pattern on bare substrate, b) Diffraction pattern after deposition, c) Intensity during deposition for the middle diffraction spot

The RHEED pattern after growth of DSO-L as seen in figure 4.1 shows some Kikuchi lines which indicate a perfect crystal with a small amount of defects. This is a good indication of a successful deposition. The intensity oscillations allowed for a clear determination of laser pulses needed for complete growth. The amount of pulses used was 3650 to grow 12 nm of SMO

(a) Before

(b) After

(c) Diffraction spot intensity

Figure 4.2: RHEED of DSO-H, a) Diffraction pattern on bare substrate, b) Diffraction pattern after deposition, c) Intensity during deposition for the middle diffraction spot

The RHEED pattern of DSO-H as seen in figure 4.2 does not show clear Kikuchi lines after growth. This could indicate the growth being less crystalline than the low oxygen DSO. The spots are also closer to streaks after growth. The intensity oscillation are clear for a large region giving rise to a clear indication of laser pulses needed. The amount of pulses used was 3900 to grow 12 nm of SMO

4.1.1.2 Atomic Force Microscopy

(a) Substrate

(b) After deposition
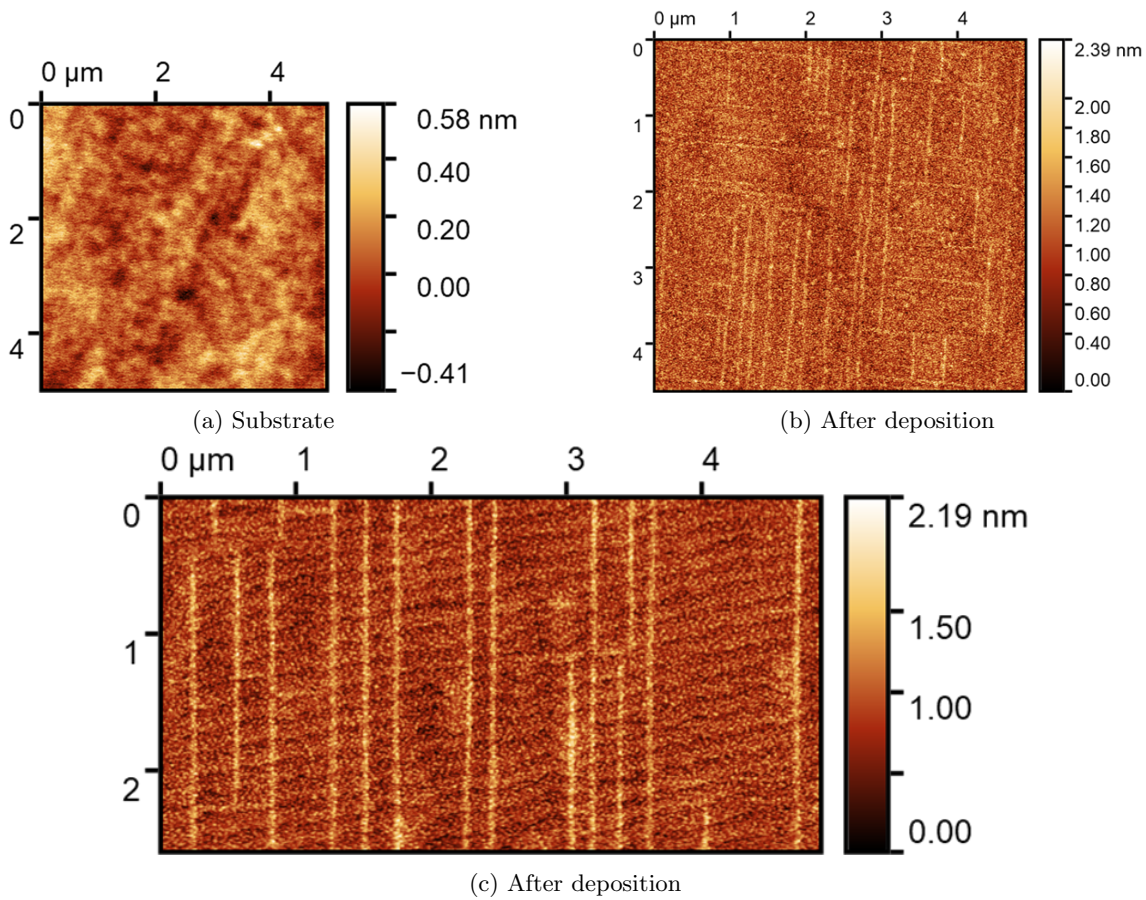
(c) After deposition

Figure 4.3: AFM images of DSO-L, a) Bare DSO substrate before annealing, b) After SMO deposition, c) After SMO deposition rotated

The AFM images of DSO-L seen in figure 4.3 reveal some interesting structures. The bare substrate (a) had a roughness of 113 pm which is smooth and does not show a clear terrace structure. The after deposition image (b) shows height lines across the sample, between these lines the roughness is around 200 pm, this is still a low roughness. The exact origin of the height lines is unclear but these might be domain walls. Other research shows resistance changes in square areas on SMO films [17]. These two phenomena might be connected possibly meaning the SMO film shows ferroelectric domains. The Lines are not an AFM artifact since (c) is a image of the rotated sample and the lines follow the rotation. The image also shows that the sample has grown with terraces while these where not present on (a). There where no AFM images taken after annealing before deposition it might be that the terraces already formed during this annealing.

(a) Substrate

(b) After deposition

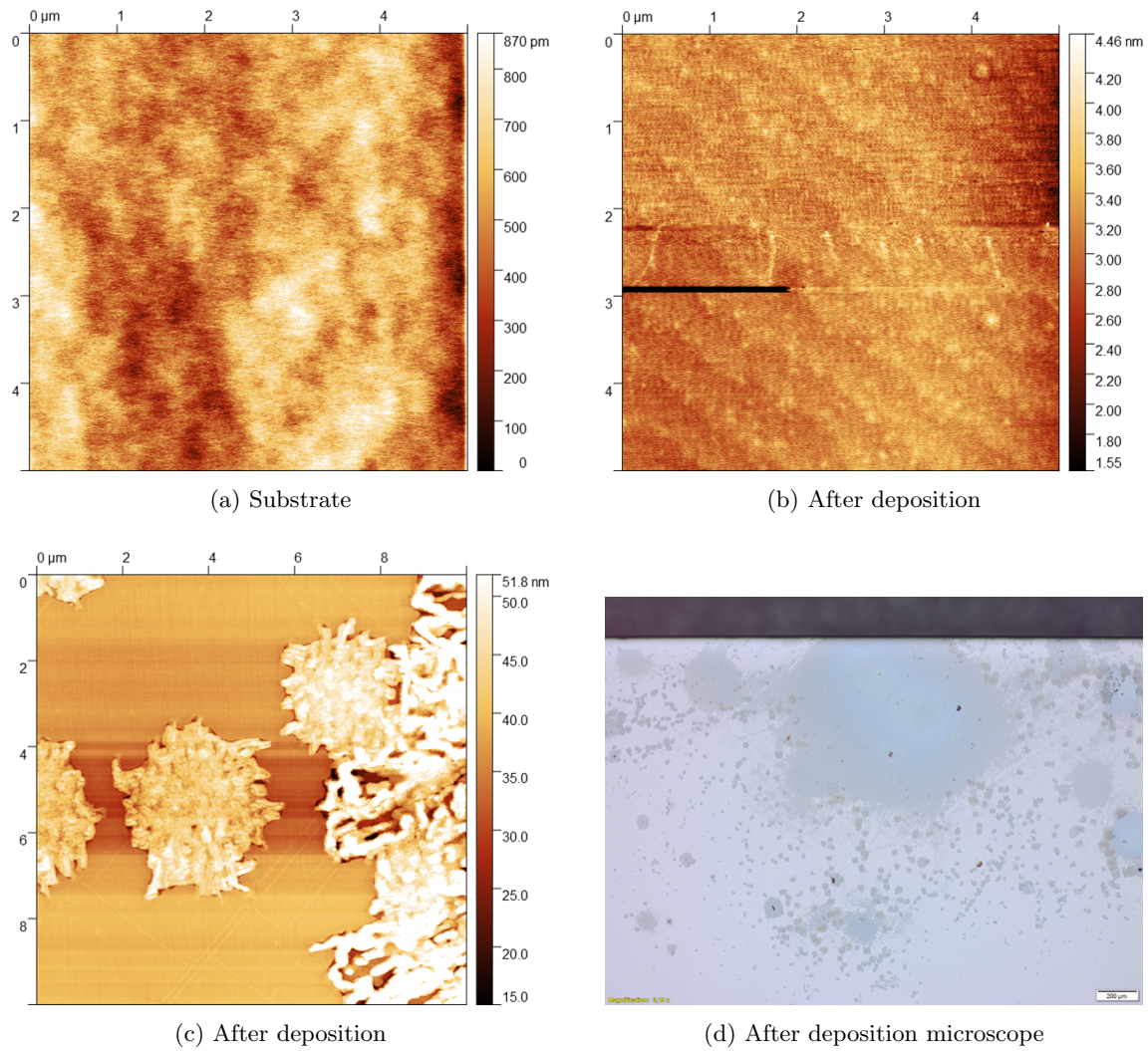(c) After deposition

(d) After deposition microscope

Figure 4.4: AFM and microscope images of DSO-H, a) Bare DSO substrate after annealing, b) After SMO deposition on homogeneous corner, c) After SMO deposition near blue area, d) optical microscope image of side of the film

The optical microscope and AFM images of DSO-H can be seen in figure 4.4. The bare substrate after annealing (a) does not show any terraces and is very flat, the roughness is 128.8 pm. AFM images not included in this thesis indicated the sample to be unclean after deposition thus the sample was cleaned. The cleaning was done with lenspaper and ethanol. The lenspaper was wet with ethanol and streaked to one side of the sample. The sample was after this submerged in ethanol and vibrated in a ultrasonic bath. Next the sample was rotated by 90° and the streaking and vibrating was repeated. This was done four times. After this process microscope images (d) where taken showing a blue region on the surface of the sample. AFM images near this region (c) reveal that this blue region is some other phase which is likely also SMO. The height differences are big giving rise to a roughness of around 5 nm on the different phase areas. AFM images where also taken some distance apart from the blue area on the corner of the sample (b). This corner looked like it was still just one phase. The AFM near this area does look more as expected. The roughness is 220 pm and it also shows some structures that look like terraces. The image has a distorted area in the middle due to some problem with the AFM imaging but the roughness did not include this area. This new phase might have been due to some thermodynamic process as a result of the high oxygen pressure and temperature during annealing.

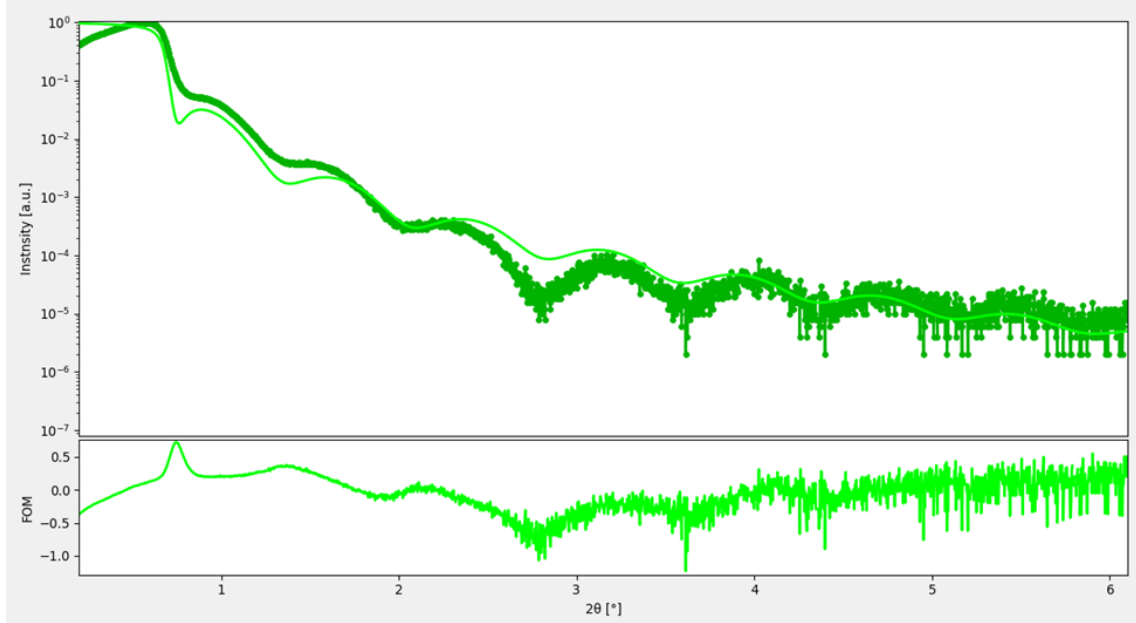### 4.1.2 Structural characterization

4.1.2.1 X-Ray Reflection

Figure 4.5: XRR fit of DSO-L

SMO film thickness	114.03898363511016 Å
SMO density	0.01572306280569594 FU/Å^3
SMO surface roughness	1.3316001014227494 Å
Interface roughness	3.533122971434464 Å
DSO density	0.016666339592486652 FU/Å^3

Table 4.2: fitted parameters XRR DSO-L

The XRR fit of DSO-L as seen in figure 4.5 is not a very good fit. An important part of the fit is the amount of oscillations since these indicate the film thickness. The amount of oscillations and the spacing of the oscillations do seem to align fairly well. The film thickness seen in table 4.2 does agree well with our expected value due to RHEED of 12 nm.
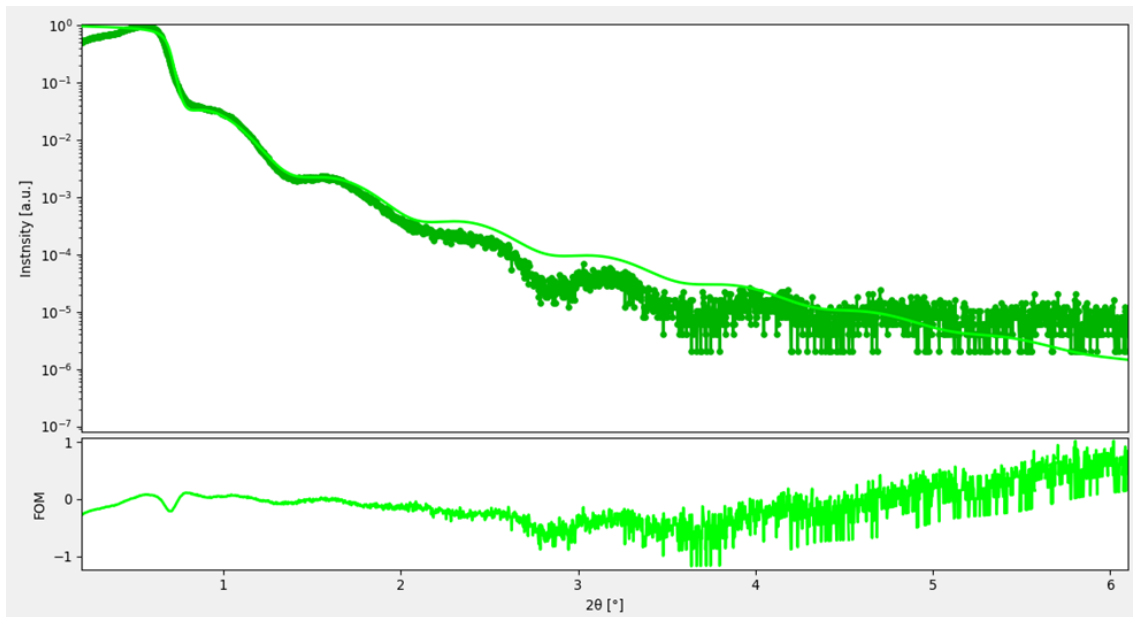
Figure 4.6: XRR fit of DSO-H

SMO film thickness	114.441 Å
SMO density	0.017668229418532296 FU/Å^3
SMO surface roughness	3.059714345756924 Å
Interface roughness	5.448397891272365 Å
DSO density	0.01745036798917133 FU/Å^3

Table 4.3: fitted parameters XRR DSO-H

The fit for the DSO-H XRR as seen in figure 4.6 is accurate up until $2\theta = 2°$ after which the oscillations become slowly more unclear. The fit shows a film thickness close to 12 nm as can be seen in 4.3 this is also the expected value from the RHEED.

4.1.2.2   X-Ray Diffraction
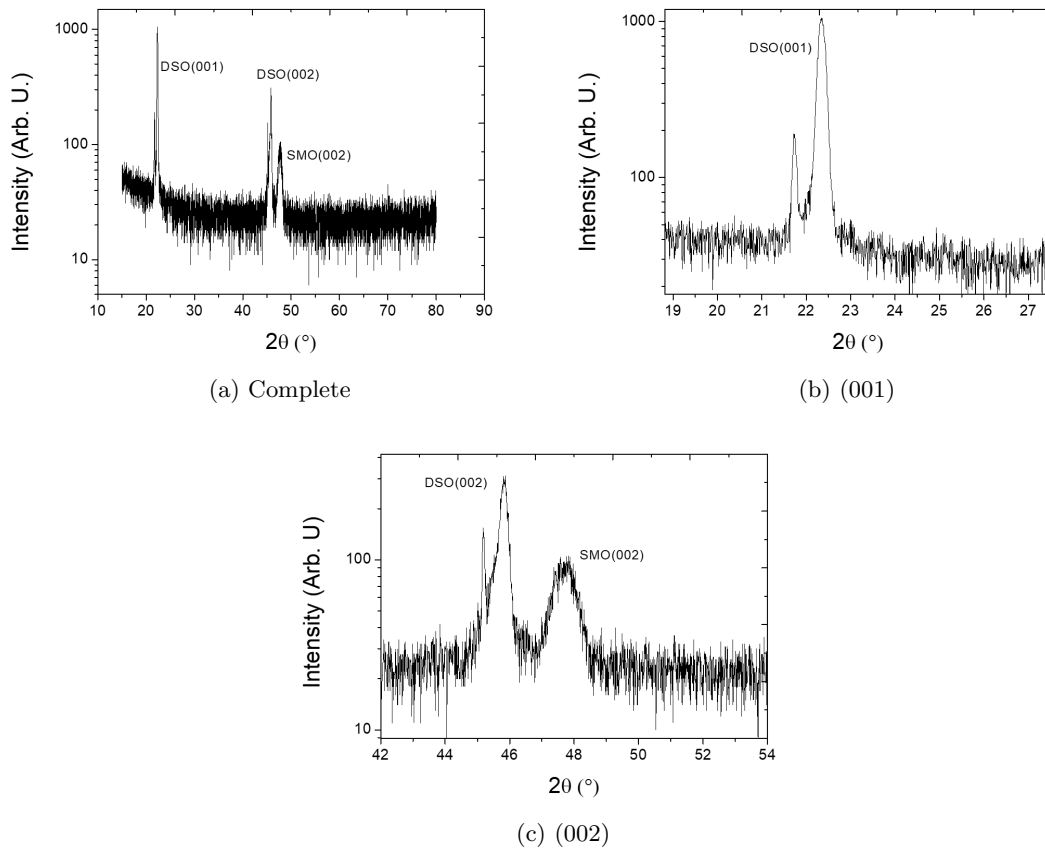

(a) Complete

(b) (001)

(c) (002)

Figure 4.7: XRD graphs of DSO-L, a) DSO-L XRD complete spectra, b) XRD zoom near DSO(001) pseudo-cubic, c) XRD zoom near DSO(002) pseudo-cubic

The XRD of DSO-L in figure 4.7 reveals that the substrate peaks have have a small second peak at a slightly lower 2θ. This is an effect due to a misalignment of the XRD device. After these results the XRD where redone at a later stage and these do not show the split peaks that are seen here. These graphs are not included due to time constraints. The SMO(002) peak in (b) suggests that $\epsilon = 0.07\%$ out-of-plane. This positive strain is most likely an indication of the slight misalignment and thus it is expected that there is no out-of-plane strain present. It could also be that the misalignment was a big influence and that the results should not be used. This result is unexpected and will be discussed further utilising the RSM data. Something to note about this and all the other XRD data is that the SMO(002) peaks are always the most discernible. This might be due to the (002) peak consisting out of diffraction of both the (001) and the (002) planes. Where the diffraction of the (001) planes uses double the path length difference of the (002) and thus has n=2. These are also the planes that contain all of the atoms of our perovskite leading to a higher intensity diffraction peak possibly.
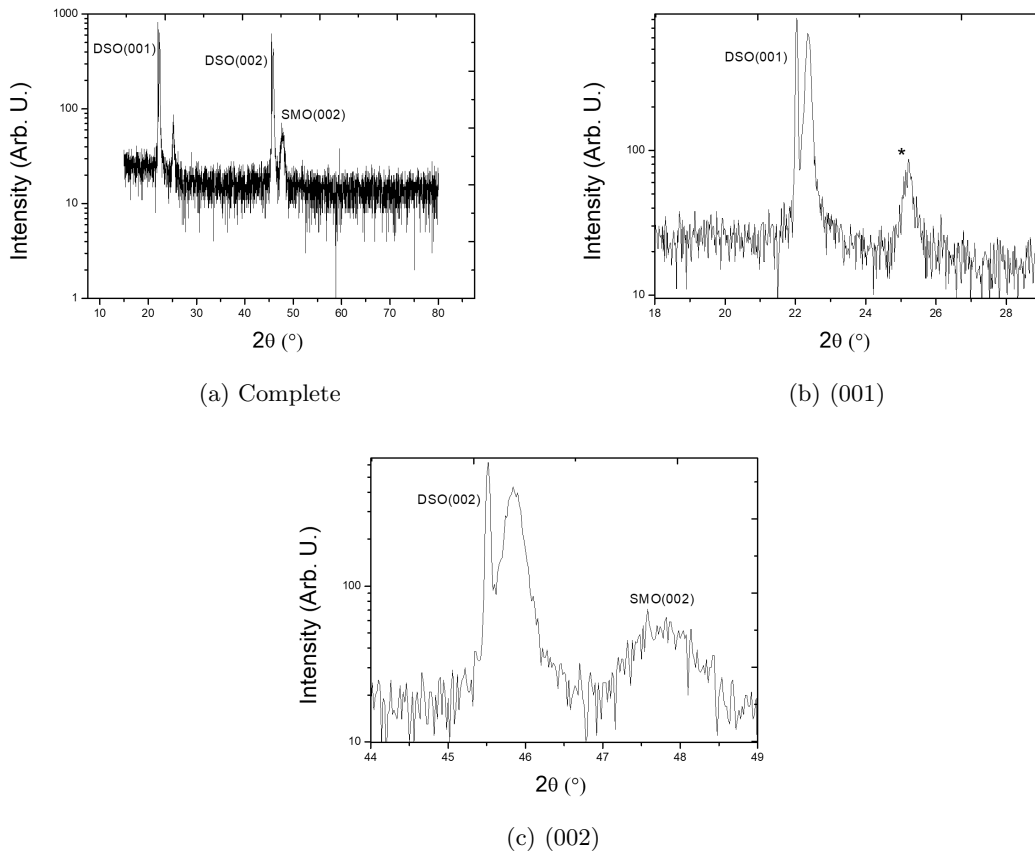
(a) Complete

(b) (001)

(c) (002)

Figure 4.8: XRD graphs of DSO-H, a) DSO-H XRD complete spectra, b) XRD zoom near DSO(001) pseudo-cubic, c) XRD zoom near DSO(002) pseudo-cubic

The XRD of DSO-H can be seen in figure 4.8 where in (b) we see this splitting of the DSO peak again and a peak denoted by *. The * peak does not seem to correspond to any expected crystal plane. The lattice parameter for this peak, assuming that this is a (001) peak, is 3.531 Å. If this peak is due to DSO (001) it would mean an $\epsilon = -7.2\%$ out-of-plane strain which is larger than the expected value of of $\epsilon = -1.63\%$ by a large amount. This peak might be due to the unexpected phase seen in figure 4.4 (c) and (d). The peak is relatively large so if this is some other contamination of the film this should probably be visible on the film which is not the case. Also no clear SMO(001) peak is discernible. It could be the case that this is SMO(001) peak on a unexpected direction due to the misalignment problem. The DSO(002) peak seen in figure 4.8 (c) has again this splitting due to some misalignment and also shows a SMO(002) peak this peak has a strain of $\epsilon = -0.07\%$ out-of-plane just like DSO-L. This means the SMO seems to be completely relaxed out-of-plane. This will be discussed more with the RSM data.

4.1.2.3   Reciprocal Space Map
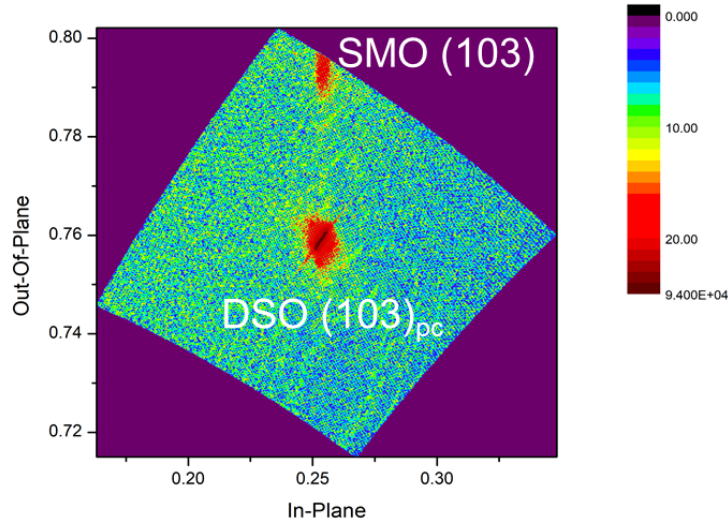
(a) DSO-L
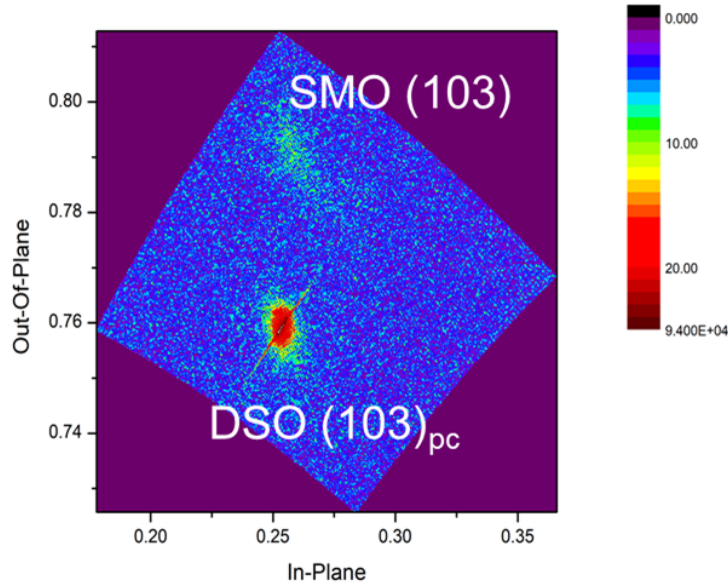
(b) DSO-H

Figure 4.9: RSM around DSO (103) pseudo-cubic, a) DSO-L RSM, b) DSO-H RSM

The RSM data presented in figure 4.9 shows some interesting results. The DSO-L (a) shows a clear SMO(103) peak although the SMO peak is not entirely on the RSM because the peak was slightly out of the measurement range. The peak already seems clear enough to estimate the strain of SMO(103). $\epsilon_x = 3.285\%$ and $\epsilon_z = -0.735\%$ This means that in-plane the SMO is strained but not quite as much as the expected 3.78% and the out-of-plane strain is even lower, only about half of the expected value of -1.63. These results are peculiar since the XRD of this sample in figure 4.7 suggested the SMO to not be strained. The RSM data is hard to explain since if this low strain is due to partial relaxation of the film then, the SMO peak should still be on the expected value but some higher intensity peaks will show to the bottom right of this SMO fully strained peak indicating some relaxed SMO. It is likely that the data for the XRD is disagrees by so much due to the misalignment thus the data for the XRD should not be trusted. Although the data does not agree with one another, the RSM peak can only be explained by some straining of SMO so it is assumed the SMO is strained on DSO-L.

A general note about all the RSM data is that the substrate peaks often show intensity lines going through them as can be seen in figures 4.9 and 4.17. These lines are an artifact of the RSM data collection and not due to the substrate exhibiting unexpected behaviour.

The DSO-H RSM in figure 4.9 (b) is a clear indication of a non-crystalline growth. The RSM shows a slightly higher intensity close to the expected SMO(103) but the area is low in intensity and not confined to a peak. This indicates not a lot of SMO to be grown crystalline and that the film is also already relaxed for some of the SMO. It is expected that a large portion of the SMO is involved in the other SMO phase present on the film as seen in figure 4.4 (c),(d) further explaining the low intensity seen in the RSM.

4.1.3 Summary

The RHEED of DSO-H seemed normal so the growth is expected be similar to the DSO-L. It can however be concluded from AFM that the film is not entirely consisting out of the expected SMO phase. We assume that during annealing the film adopted a new partial phase. We believe this to be the consequence of some thermodynamic process induced by the high temperature and pressure. It could be that this non-epitaxial phase was created while cleaning or handling the thin film. This does not seem likely since slight mishandling of the film and possible accidental scratching with tweezers do generally not affect the film to such an extend. Ethanol used to clean the film should also not have influenced the film and if it did the same effect would be expected for the entire film not just discrete spots. Ethanol is also often used on SMO and is not known for creating reactions with SMO. The DSO-L does show a well grown epitaxial film and is strained as confirmed by RSM. Following these results and due to time constraints the DSO samples where not further examined.

4.2 SrMnO$_3$ on SrTiO$_3$

4.2.1 Growth characterization

Similar to our SMO on DSO samples, two thin films where grown. A low and a high oxygen annealing sample which are called DSO-L and DSO-H respectively. STO-L was exposed to 100 mbar of oxygen pressure whilst annealing while STO-H was exposed to 1 bar of oxygen pressure. Both STO samples underwent a chemical protocol to make it TiO$_2$ terminated. The chemical used for termination was buffered hydrofluoric acid(BHF) which reacts with the SrO present on the top layers and thus leaves us with the TiO$_2$ surface without SrO. After this the substrate is annealed for 90 minutes at 1000°C with a steady oxygen flow. The temperature of the sample holder during deposition was 800°C and the oxygen pressure during deposition was $5 \cdot 10^{-2}$ mbar. The pulsed laser used was a Krypton Fluoride laser with a wavelength of 248 nm. The fluence of the laser was 2 J/cm^2 and the pulse frequency was 5 Hz. The annealing after deposition was done at 600°C for 1 hour long. After which it was cooled to room temperature at a rate of 10°C per minute. The amount of pulses needed to grow about 30 unit cells or 12 nm was for the STO-L 4000 and STO-H needed 3600. The STO substrates have a (001) orientation.

4.2.1.1   Reflection High-Energy Electron Diffraction

(a) Before

(b) After
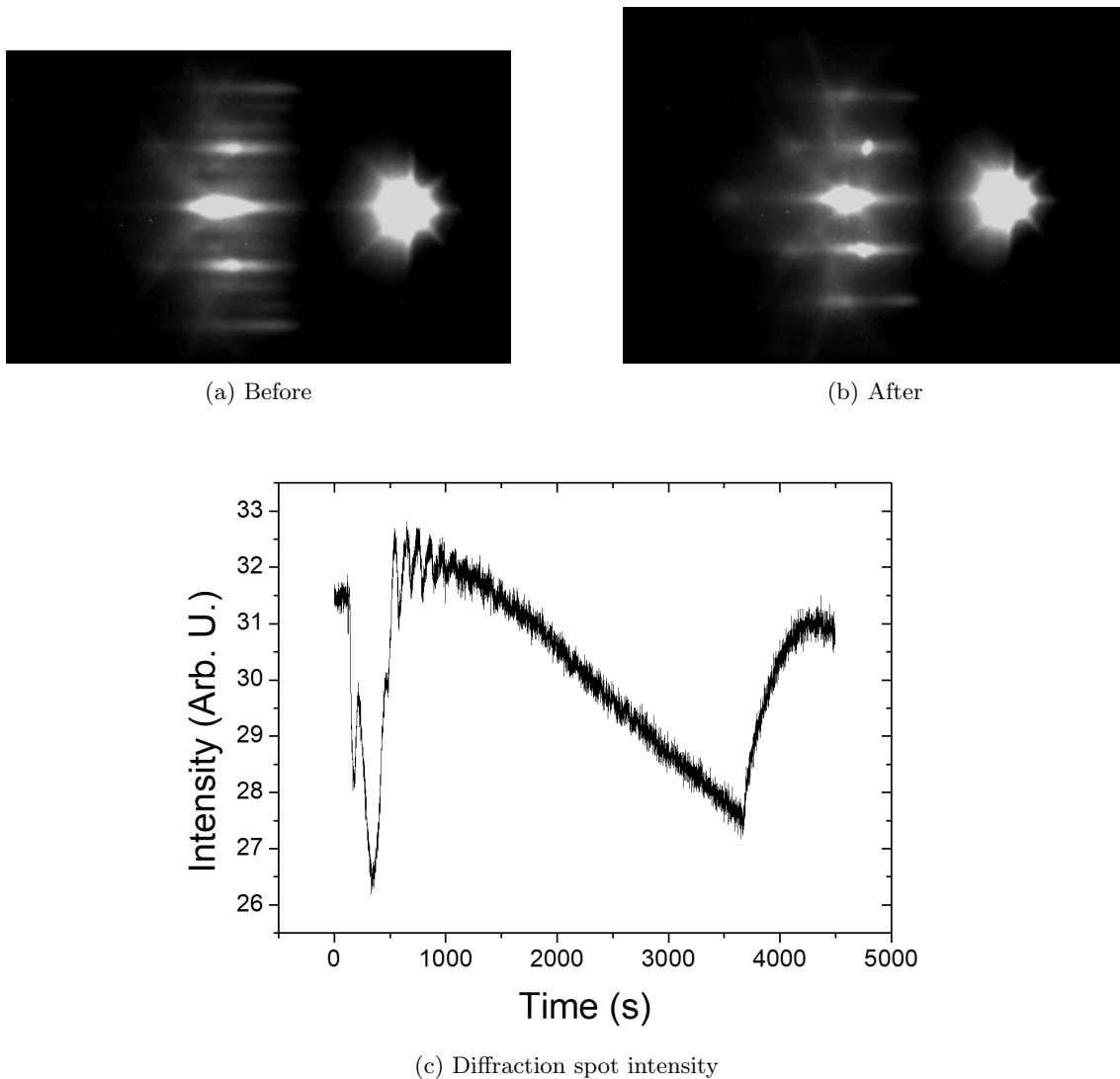

(c) Diffraction spot intensity

Figure 4.10: RHEED of STO-L, a) Diffraction pattern of bare substrate, b) Diffraction pattern after deposition, c) Intensity during deposition for the bottom diffraction spot

The RHEED images of STO-L seen in figure 4.10 show kikuchi lines before and after growth. This is something not observed on both of the DSO samples. It could be that DSO does not show the lines because of its pseudo-cubic structure but when the SMO grows crystalline they might still appear. The RHEED in figure 4.10 (c) shows some drops before it starts oscillating. This might be due to the diffraction being unclear because the SMO growth at the interface does not create similar crystal planes spacing as the STO substrate. As more SMO is deposited the X-rays diffract of multiple layers of SMO which should have similar crystal plane spacing. This we can see in (c) after the initial drops the intensity starts to oscillate well. These oscillation where extrapolated to determine the pulses needed for a 12 nm film which where found to be 4000.

(a) Before

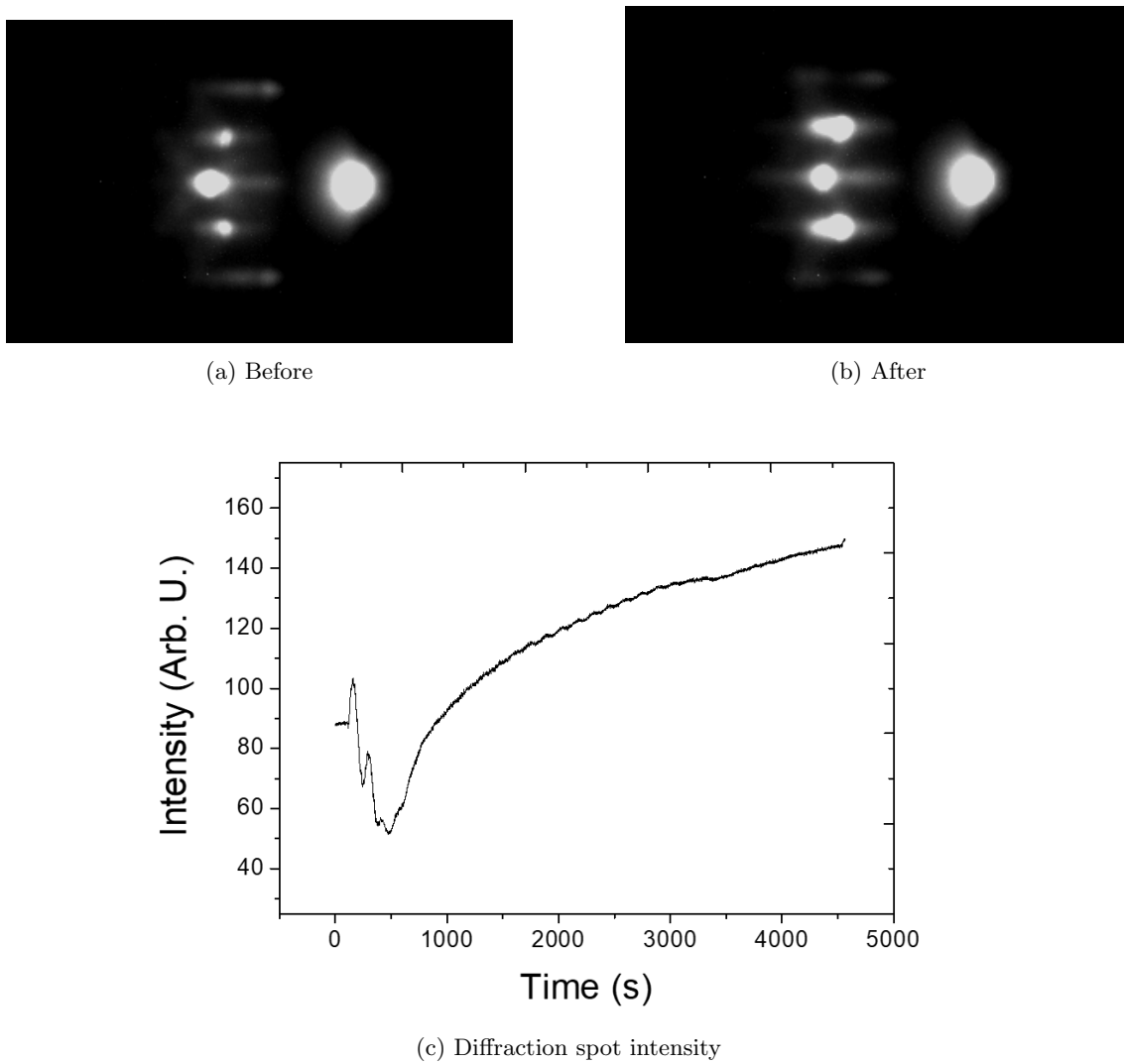
(b) After

(c) Diffraction spot intensity

Figure 4.11: RHEED of STO-H, a) Diffraction pattern of bare substrate, b) Diffraction pattern after deposition, c) Intensity during deposition for the middle diffraction spot

The STO-H growth does not contain very big RHEED oscillations as shown in figure 4.11. While the oscillations are not that big they are still noticeable and usable for the extrapolation for the pulses needed to grow 12 nm, the amount of pulses needed for this film was 3600. We can again notice that the signal at the beginning drops which is probably because of the mismatch in crystal plane spacing at the interface. Kikuchi lines seem to be a bit less clear than the STO-L sample as seen in figure 4.10(a) (b). This is probably due to a slightly different alignment or RHEED intensity.

4.2.1.2 Atomic Force Microscopy

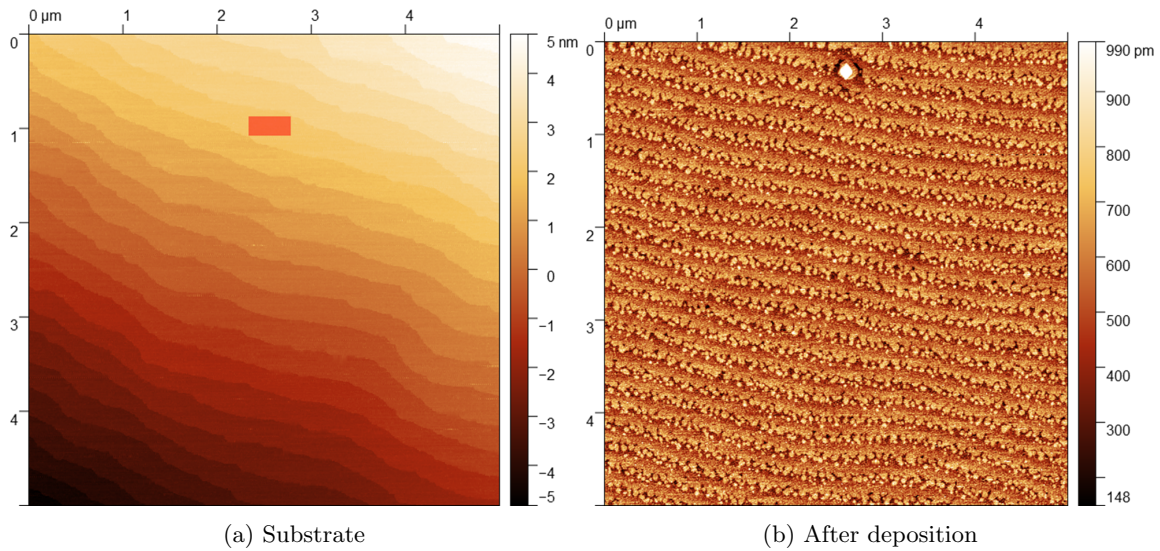(a) Substrate   (b) After deposition

Figure 4.12: AFM of STO-L, a) Bare STO-L substrate after chemical protocol and annealing , b) STO-L after deposition

The substrate of STO-L shows very clear terraces before the deposition as seen in figure 4.12 (a). The roughness on the terrace indicated by the red rectangle is 73 pm and the other terraces give similar values. This is a very flat substrate. The AFM after deposition (b) has retained the terrace structure but has introduced some small islands close to the terrace edges. The islands are of the same height as the terraces which lead to the low roughness of 133 pm after growth. The roughness even goes down to 54 pm when analysing one terrace. The AFM data indicate a 2 dimensional growth. The AFM images show extremely different height scales, this is a consequence of how the data is plotted. Image (a) is plotted by altering the data such that the terraces are flat. This is done to show that the height decreases with every terrace step. While image (b) is plotted such that the height differences are as small as possible. This gives bigger contrast to the terraces and their edges that show interesting features.

(a) Initial substrate

(b) After BHF

(c) After annealing
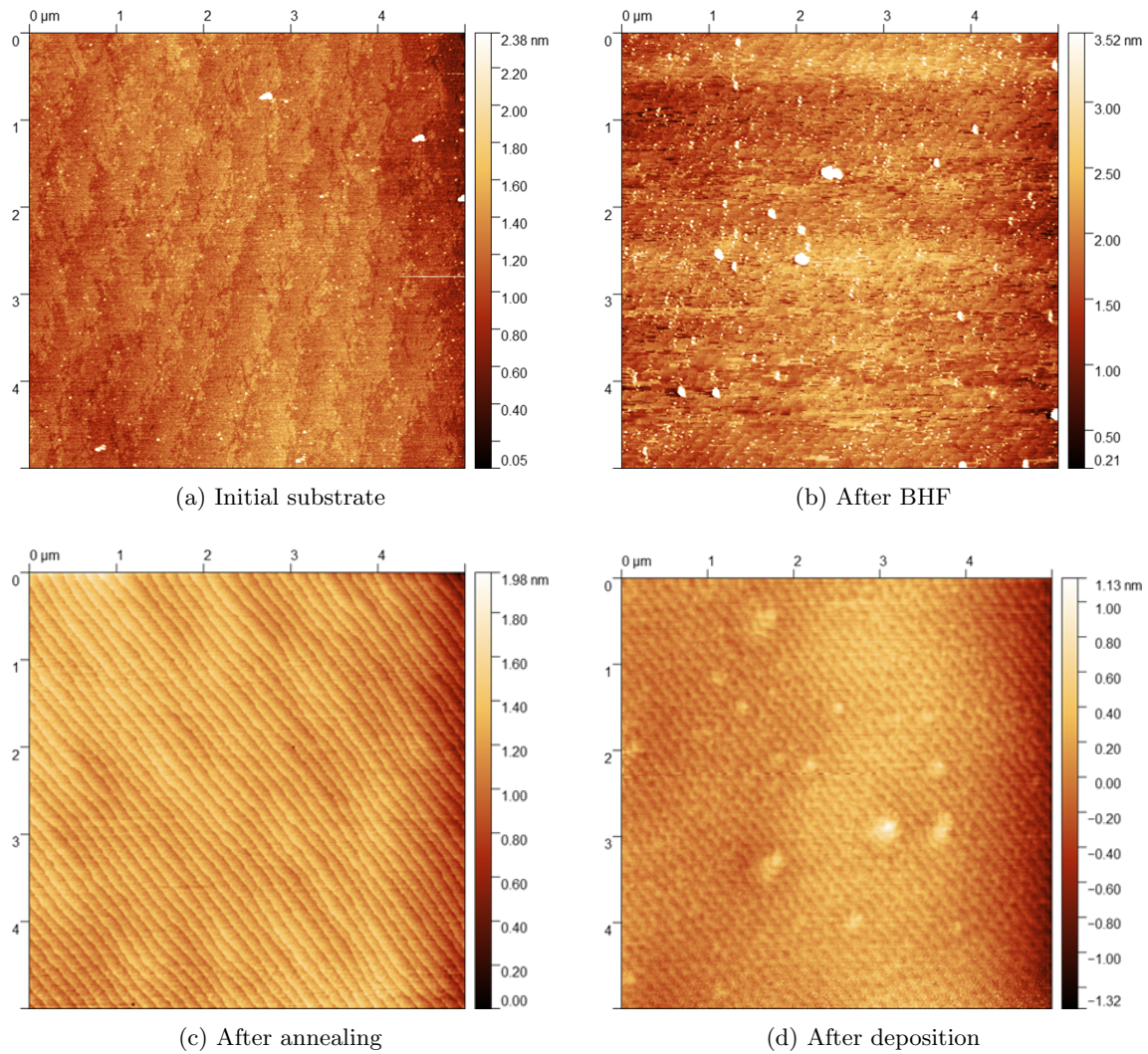
(d) After deposition

Figure 4.13: AFM of STO-H, a) Bare STO-H substrate before any process, b) STO-H after undergoing chemical protocol, c) STO-H annealed, d) STO-H after deposition

The AFM images of STO-H can be seen in figure 4.13. The initial substrate (a) shows some structure that resembles a terrace structure but comparing it with (c) shows that the terraces should be smaller than (a) shows. The roughness of (a) is 267 pm. The roughness after the substrate had undergone the chemical protocol (b) is 850 pm when including the many peaks and becomes closer to 350 pm when leaving these out. It shows that the chemical protocol has definitely impacted the substrate. In (c) the surface after annealing is shown. The film now shows a clear terrace structure. The difference between the AFM images show the importance of the process before deposition. The roughness of (c) is 124 pm. The thin SMO film seen in (d) shows terraces which further confirms that the growth is 2 dimensional. The roughness of (d) is 134 pm and includes some small peaks. They might be indications that the film is beginning to grow a bit 3 dimensional but the highest peaks are about 0.8 nm high meaning that the peaks are 2 unit cells high and only consist of a small amount of SMO. Overall this should still be a epitaxial film.

4.2.2 Structural characterization
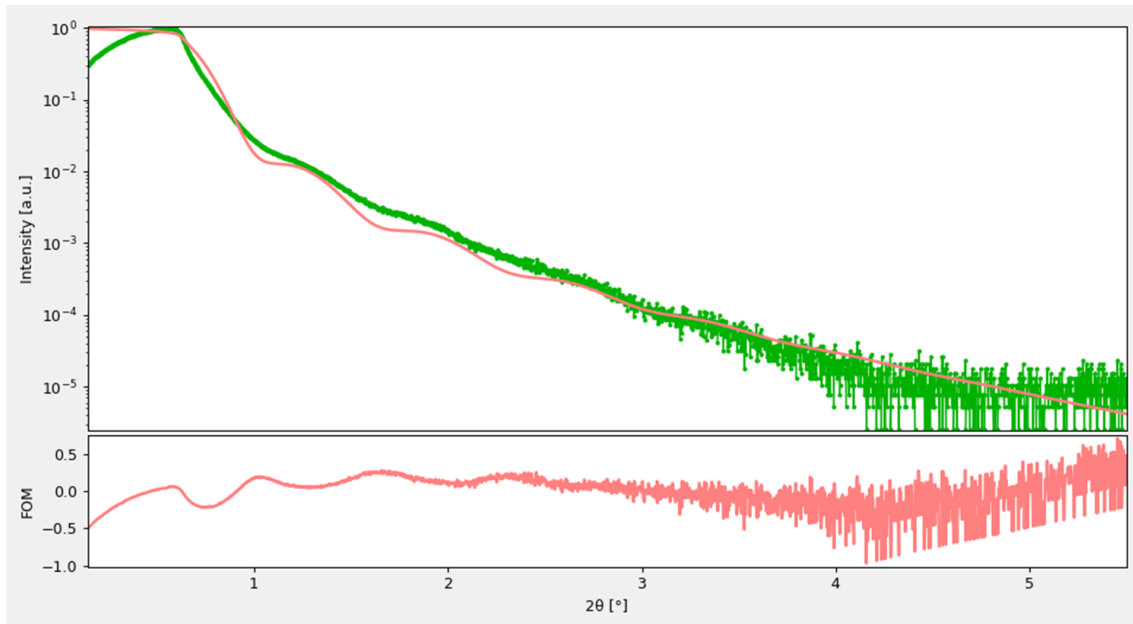
4.2.2.1 X-Ray Reflection

Figure 4.14: XRR fit of STO-L

SMO film thickness	119.522 Å
SMO density	0.02047367 FU/Å^3
SMO surface roughness	3.038688 Å
Interface roughness	0.8797243 Å

Table 4.4: fitted parameters XRR STO-L

The XRR data of STO-L seen in figure 4.14 does not show very clear oscillations and does not match the fit very well. The small oscillations for the smaller angles do have similar spacing to the fit so it is expected that the thickness result is still adequate. The film thickness in table 4.4 is again close to 12 nm as expected.
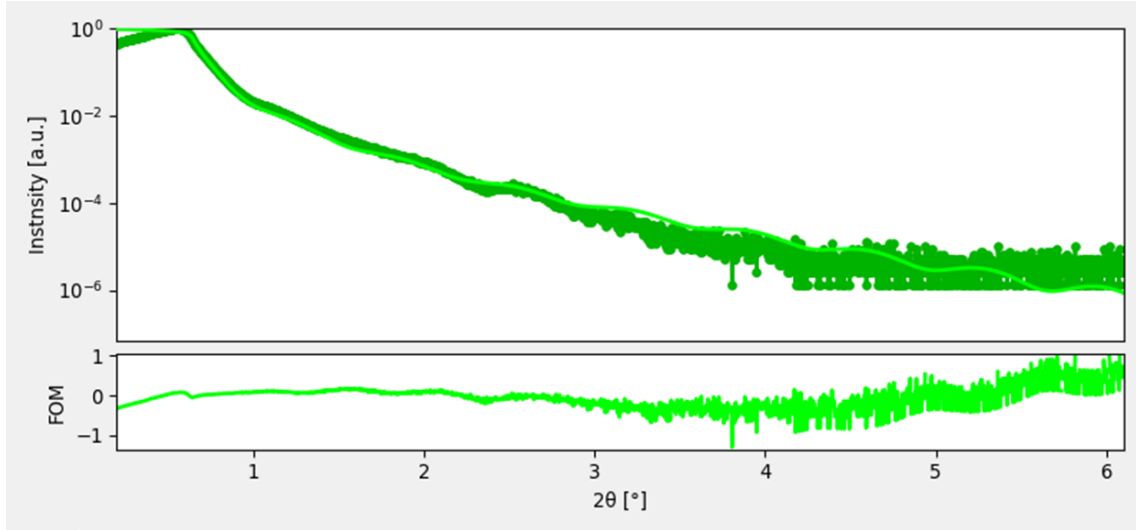
Figure 4.15: XRR fit of STO-H

| SMO film thickness	126.5590159086826 Å
SMO density	0.018361960530222488 FU/Å^3
SMO surface roughness	3.6871910403167947 Å
Interface roughness	0.8778479575665473 Å
STO density	0.01775804609077539 FU/Å^3

Table 4.5: fitted parameters XRR STO-H

The XRR data of STO-H does not show clear oscillations as seen in figure 4.15. The oscillations are hard to distinguish but seem to overall agree with the fit. The film thickness seen in table 4.5 does again agree with the expected 12 nm. The XRR of both STO samples are not very clear this could be a result of the density being very similar for the deposited material and substrate or the interface roughness being high. The density are similar for the STO and SMO for STO-H in table4.5 but the same is true for DSO-H in table 4.3 while it shows clear oscillations in figure 4.6, while the interface roughness is also high for DSO-H and low for STO-L.

4.2.2.2 X-Ray Diffraction
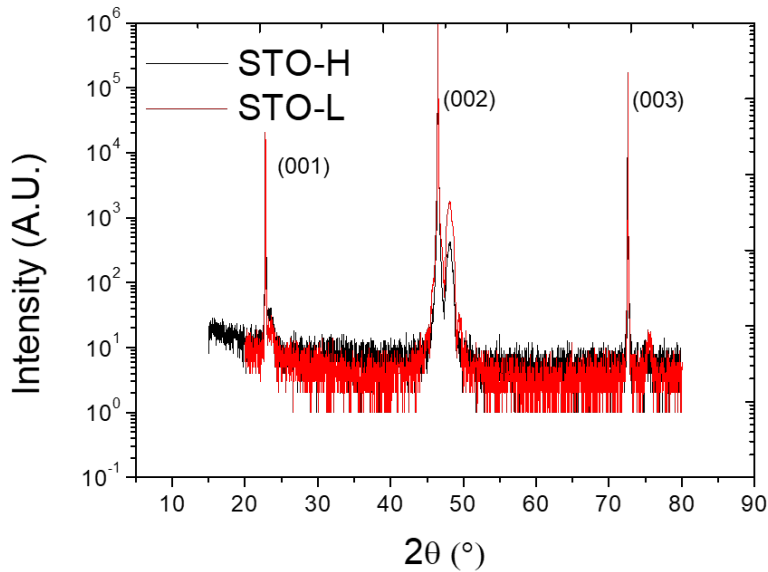
(a) complete range
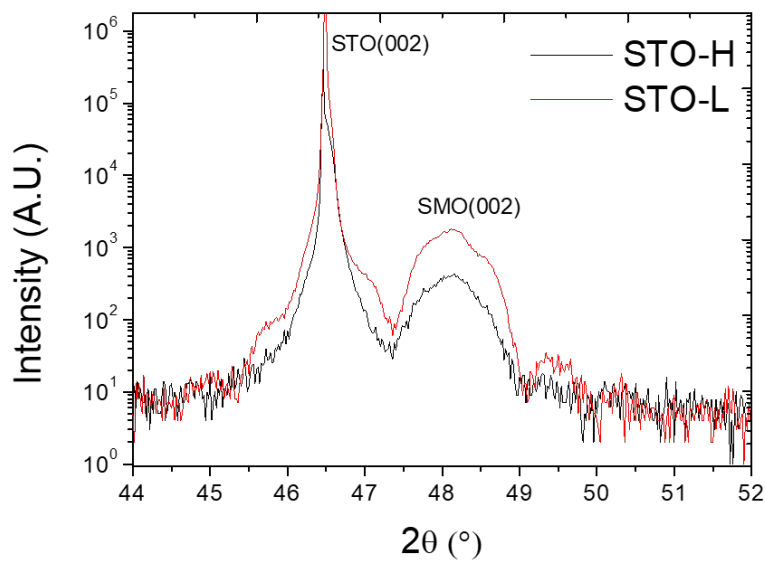
(b) (002)

Figure 4.16: XRD graphs of STO-L and STO-H, a)The complete spectra , b) Zoom near STO(002)

In figure 4.16 (a) the XRD spectra of STO-L and STO-H are shown where (b) shows the zoom around (002) because this region shows clear SMO peaks for both of the samples. It is clear from (b) that the strains of STO-L and STO-H are very similar. Using the (002) peaks, STO-L gives a strain of $\epsilon = -0.80420\%$ out-of-plane and STO-H gives a strain of $\epsilon = -0.64914\%$ out-of-plane. This means that the both are not stained as much as the expected expected $\epsilon = -1.29\%$ [11]. This will be discussed more with the RSM data. The films show fringes in the XRD indicating a crystalline film. The fringes are shown for both samples on the right of the SMO(002) peak but the peaks of STO-L are a bit clearer. STO-L also shows a fringe between the STO(002) and SMO(002) peak. Suggesting STO-L has less structural defects.
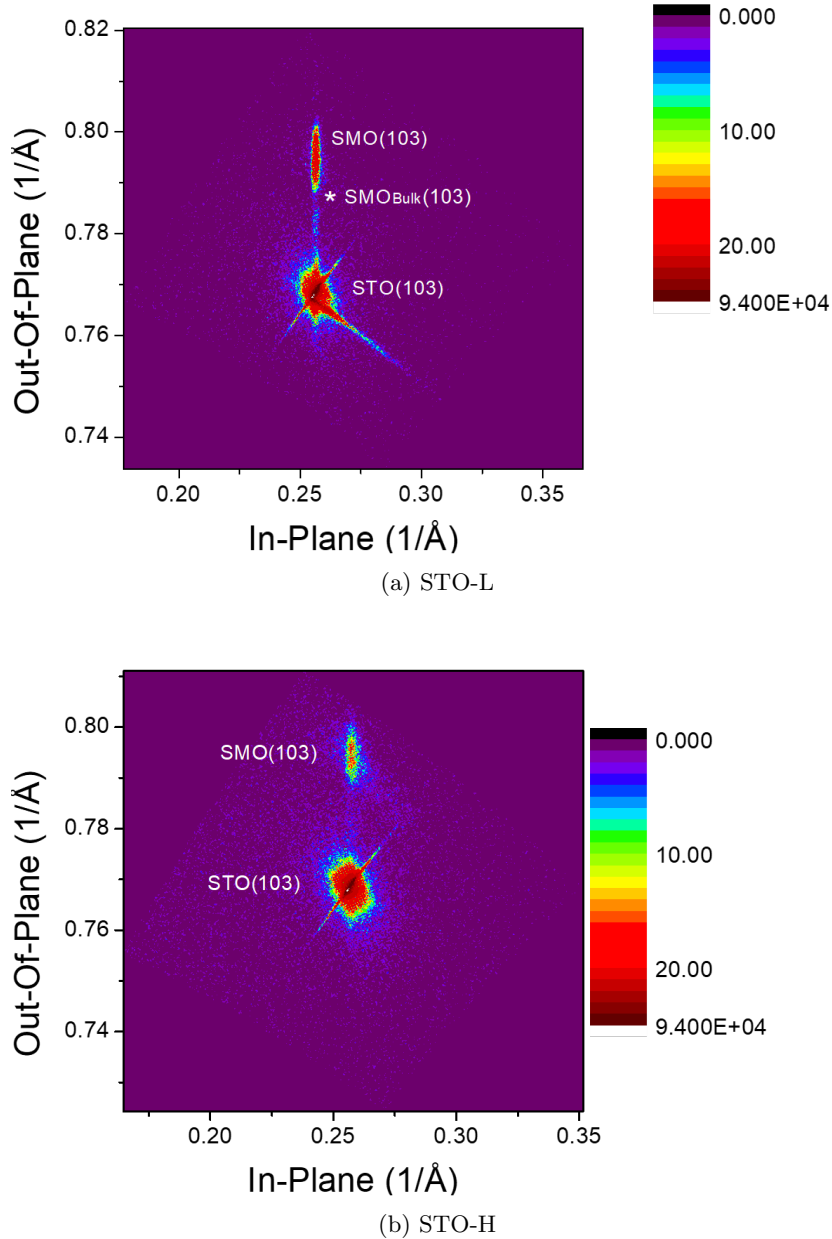
4.2.2.3   Reciprocal Space Map

(a) STO-L

(b) STO-H

Figure 4.17: RSM around STO (103), a) STO-L RSM where $SMO_{bulk}(103)$ indicates where unstrained SMO(103) would reside, b) STO-H RSM

The RSM of the STO samples are shown in figure 4.17 and they show a similar result for STO-L and STO-H. STO-L (a) is strained and shows no signs of relaxation. STO-H (b) is also strained but some of the film is relaxing indicated by the small dots straying away from the SMO(103) peak towards the bottom right $SMO_{bulk}(103)$ position in reciprocal space. The lattice parameters and strain found using the RSM are collected in table 4.6. The strains are again lower than expected. The expected strain for STO-L is $\epsilon = 2.63\%$ out-of-plane. The STO-L could still be fully strained if we consider a read off error however, the out-of-plane strain is expected to be $\epsilon = -1.29\%$ which is not close for STO-L or STO-H. Considering the RSM and XRD both produce results suggesting a non complete strain out-of-plane and the RSM suggesting almost complete strain in-plane it could be possible that the lattice is possibly more strained as expected out-of-plane than in-plane since the in-plane has much lower strain than expected.

	STO-L	STO-H
C(out-of-plane)	3.774 Å	3.776 Å
ϵ(out-of-plane)	-0.8147 %	-0.7622 %
A(in-plane)	3.900 Å	3.885 Å
ϵ(in-plane)	2.4967 %	2.102 %

Table 4.6: strain of SMO(103) on STO-L and STO-H by RSM

4.2.3   Summary

The STO-L and STO-H both show similar growth and structural characteristics. The STO-H seems to relax but only to a small extend. The results conclude that STO films can be grown with a higher oxygen annealing pressure. The STO films will be further analysed in the following section to determine if the oxygen vacancies have successfully been controlled.

4.2.4 Magnetic probing

The magnetization-temperature(M-T) plots involve a Zero Field Cooled (ZFC) and a Field Cooled 7 Tesla (FC7T) curve. The curves are obtained by increasing the temperature to a point where all magnetization of the sample should be lost. This is accomplished by heating the sample to 380 K. The ZFC will gradually decrease the temperature to 5K and than apply a field of 1000 Oe (100 mT) in the in-plane direction. The ZFC will now start recording magnetization data as it increases the temperature.

The FC7T will also reach 380K but will now apply a field of 7 T in-plane while the temperature decreases to 5 K. The field switches to a 1000 Oe running field and data of the magnetization will be recorded as the temperature is increased.
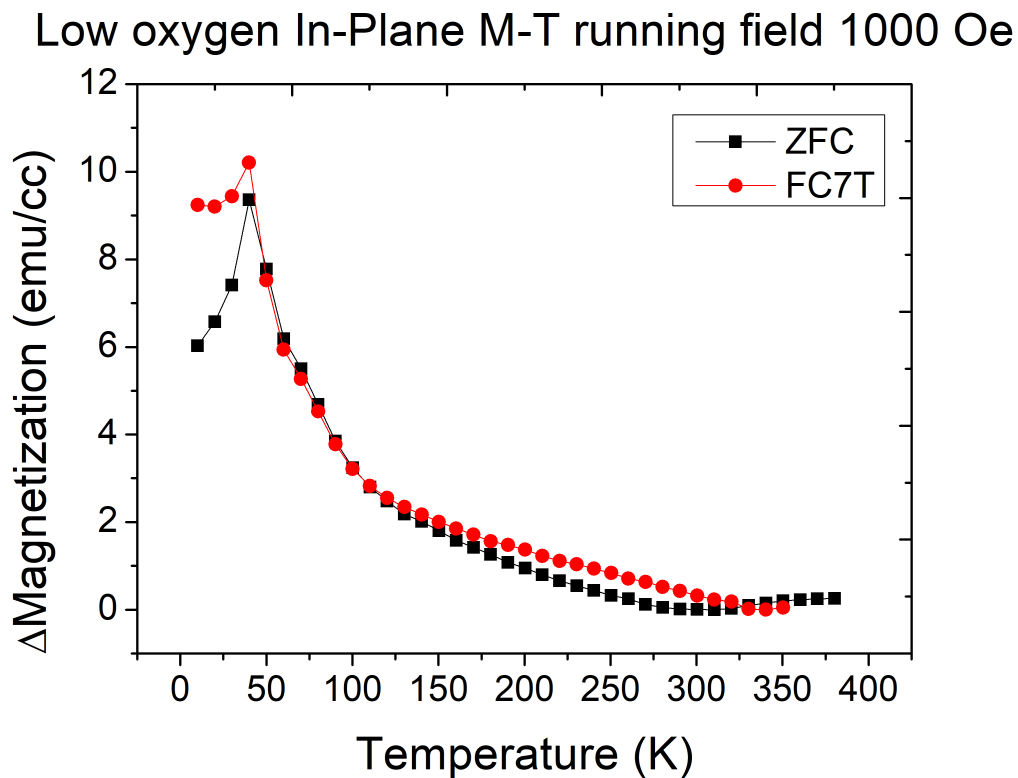

Figure 4.18: M-T curve of STO-L showing ZFC in black and FC7T in red. The ΔMagnetization is the magnetization data shifted such that the lowest point is zero

The ZFC and the FC7T in figure 4.18 both have a similar shape. The graph is clearly not a standard ferromagnetic M-T curve however, there is a clear difference between the ZFC and FC7T curve. The magnetization of the ZFC before 40 K lies lower than the FC7T. This has to be due to some magnetization still present as a consequence of the 7 T field. This suggests that there is some ferromagnetic contribution in our STO-L sample as was expected due to the oxygen vacancies that induce double exchange. It can also be noticed that the curves share similar magnetization above 40 K. This is an indication that the Curie temperature of the present ferromagnetic phase has been reached. An explanation for the difference between FC7T and ZFC has now been provided but this still leaves us with the shape of the graphs. Most of the SMO film will be antiferromagnetic due to superexchange and some of it will be ferromagnetic due to the oxygen vacancies leading to double exchange. The interpretation of the shape of the curve before 40 K is as follows. In the mostly antiferromagnetic thin film some small ferromagnetic regions are present as depicted graphically in figure 4.19. The ferromagnetic domain does not align completely with the in-plane direction. This could be because of some sort of coupling between the ferromagnetic regions and the large antiferromagnetic regions. This coupling could be due to for instance the magnetic moments being coupled or crystal lattice effects that couple the two regions in some way. The coupling decreases as temperature increases giving rise to a increase in magnetization as temperature increases. This
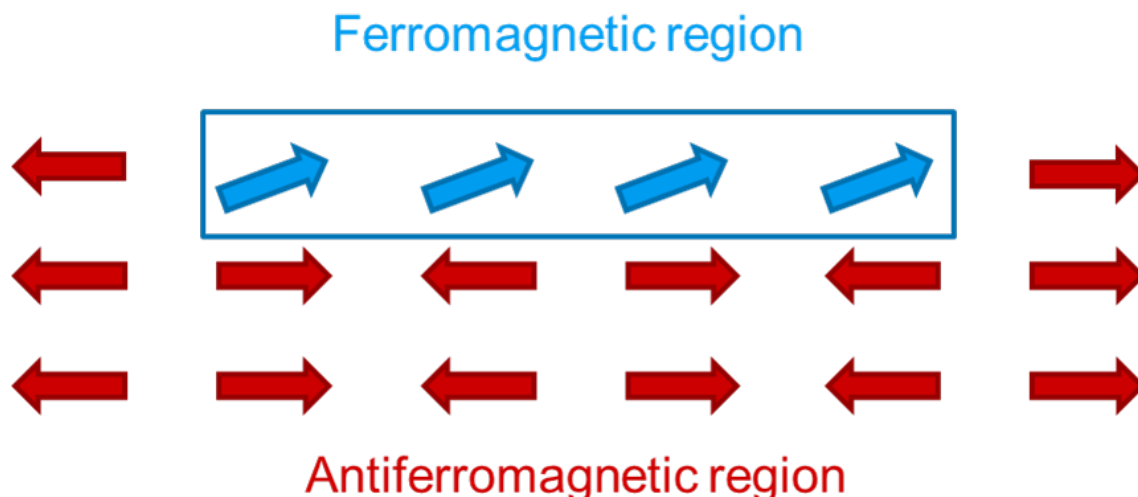
Figure 4.19: Graphical representation of STO-L before 40 K

leads to increasing magnetization until the ferromagnetic domains become unordered at the Curie temperature which will cause the magnetization to decrease. Comparing the magnetization to a regular ferromagnet which would be in the order of several 100 emu/cc reveals that most of the film should be antiferromagnetic. However no clear Néel temperature is observed. Néel temperature is often hard to distinguish because the antiferromagnetic magnetization is already so small. We do however observe the curves taking a different slope around 100 K which is lower than the expected 150 K to 160 K range for the Néel temperature seen in figure 2.5 where the phase transitions to paramagnetic. So this might not be the Néel temperature

Comparing the M-T of STO-L in figure 4.18 with STO-H in figure 4.20 we can observe that the STO-H also shows some transition around 40 K where after ZFC and FC7T overlap. The same general reasoning can be applied here as was done for the STO-L sample. The difference however is that the total magnetization is lower and that the magnetization decreases before 40 K rather than increasing. A possible explanation for the data is the same as for STO-H but with smaller or less ferromagnetic regions as can be seen in figure 4.21. The decrease before 40K could possible be explained by some paramagnetic material being present. This could even be the case for the STO-L but it might not be visible because the increase in magnetization due to the ferromagnetic phase being less coupled dominating the decrease. The effect is prevalent in both the ZFC and FC7T making it likely that it is some paramagnetism. If this would be a paramagnetic effect it will have to be caused by some other material than STO or SMO because the do not exhibit paramagnetism. The films have been in contact with silver paste that is paramagnetic in this temperature range. The films had been cleaned of silver paste before these measurements were conducted but possibly some silver paste was still present. It could be the case that this is due to a different coupling between the antiferromagnetic and ferromagnetic regions leading to a different shape for the STO-L and STO-H samples. We claimed that the lower magnetization should be due to lower amount of ferromagnetism but when comparing the magnetization difference of ZFC and FC7T this should also show a bigger difference for STO-L. This is not realy the case, the differences are similar for STO-L and STO-H while the maximum magnetization is of STO-L is more than doubled that of STO-H. It could be that the bigger ferromagnetic domains are relatively easier to magnetize than the smaller domains. Which would lead to the running field causing a slightly higher magnetization in the ZFC of STO-L leading to a smaller difference between ZFC and FC7T The magnetization shown in figure 4.18 and figure 4.20 is the Δmagnetization which means that the data is shifted such that the lowest data point is zero. This is done to lower the impact that trapped fields in the MPMS have on the data and to remove possible background contributions to the magnetic data.
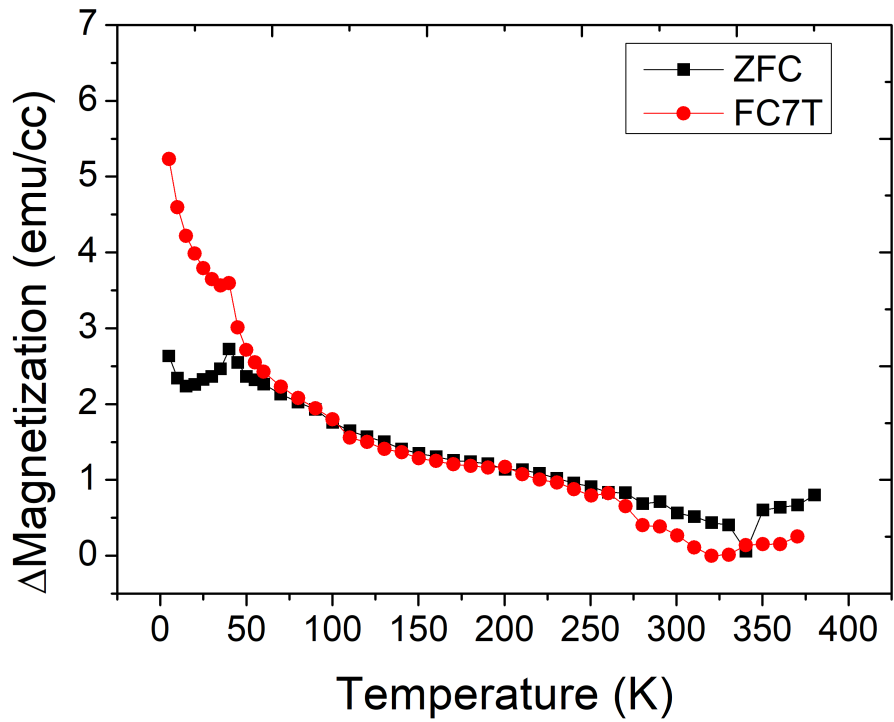
Figure 4.20: M-T curve of STO-H showing ZFC in black and FC7T in red. The ΔMagnetization is the magnetization data shifted such that the lowest point is zero
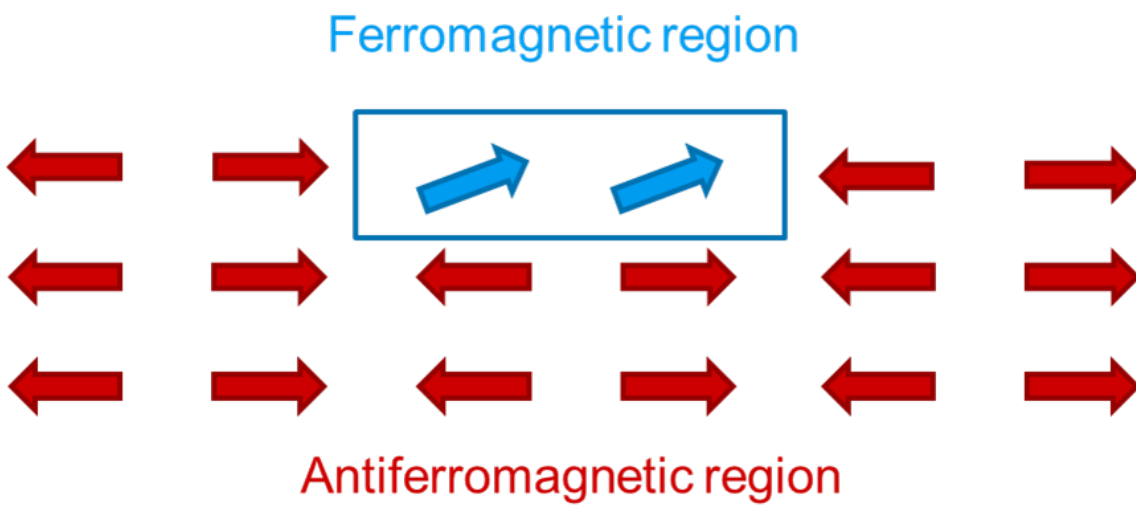

Figure 4.21: Graphical representation of STO-H before 40 K

Chapter 5

Conclusion

The SrMnO$_3$ on DyScO$_3$ or high strain films do not seem to respond well to the combination of high oxygen pressure and heat during annealing. The phase present on the film is most likely a non-epitaxial SMO phase that was created by a thermodynamic process during annealing. The outlook would be to try and grow the films with a slightly lower oxygen pressure to see if this does produce a stable film or introduce a capping layer on top of the film to structurally reinforce it. Also no clear terrace structure was observed for the DSO substrates while this was present for the STO this could lead to better epitaxial films. The STO used a chemical protocol before deposition it might be sensible to also do this for the DSO films. The DSO films can be terminated using a chemical protocol discussed here [18] after which a terrace structure can be present. The DSO samples will still be used in further research and some preliminary measurements have already been done on the films but are omitted for this thesis

The SrMnO$_3$ on SrTiO$_3$ or low strain films do seem to produce similarly strained films when 100 mbar or 1 bar of oxygen annealing pressure is used. The only indication of the actual oxygen vacancy content are the magnetization - temperature curves which do seem to indicate a smaller ferromagnetic component for the high oxygen pressure film and thus a lowering of oxygen vacancies due to a higher oxygen annealing pressure. The films are however not fully strained. This could be due to some defects in the film slightly lowering the total strain. The outlook is to conduct further research in to these SrMnO$_3$ on SrTiO$_3$ thin films, starting with more magnetic probing such as the out-of-plane magnetization - temperature curves to get a view into the possible anisotropy. Magnetization - applied field measurements could be conducted to better describe the magnetic behaviour of the films both in- and out-of-plane and give us more confirmation of an actual decrease in oxygen vacancies.

Chapter 6

Acknowledgements

Bibliography

[1] Sasikanth Manipatruni, Dmitri E Nikonov, Chia-Ching Lin, Tanay A Gosavi, Huichu Liu, Bhagwati Prasad, Yen-Lin Huang, Everton Bonturim, Ramamoorthy Ramesh, and Ian A Young. Scalable energy-efficient magnetoelectric spin–orbit logic. *Nature*, 565(7737):35–42, 2019.

[2] F. Gunkel, D. V. Christensen, Y. Z. Chen, and N. Pryds. Oxygen vacancies: The (in)visible friend of oxide electronics. *Applied Physics Letters*, 116(12):120505, 2020.

[3] Paul Tinnemans. *DyScO3 thin film substrates*. 2012.

[4] S. Blundell. *Magnetism in Condensed Matter*. Oxford Master Series in Condensed Matter Physics. OUP Oxford, 2001.

[5] Sitki Aktas. *Gas phase preparation of magnetic nanoparticle hydrosols*. PhD thesis, 10 2014.

[6] Wu Hai-Ping, Kaiming Deng, Tan Wei-Shi, Xiao Chuan-Yun, Hu Feng-Lan, and Qunxiang Li. The structural, electronic, and magnetic properties of srfeon (n 2 and 2.5): A gga+u study. *Chinese Physics B*, 18:5008, 11 2009.

[7] Q. Liu, J. Miao, Robert Reeve, Kangkang Meng, X. Xu, Y. Wu, and Yong Jiang. Ultra-large non-volatile modulation of magnetic moments in pbzr0.2ti0.8o3/mgo/la0.7sr0.3mno3 heterostructure at room temperature via interfacial polarization mediation. *Scientific Reports*, 7, 06 2017.

[8] RN Jagtap and AH Ambre. Overview literature on atomic force microscopy (afm): Basics and its important applications for polymer characterization. 2006.

[9] JocelyN Andres, Valéria Longo, L. Cavalcante, M.L. Moreira, Jose Varela, and Elson Longo. A fresh look at the structural, ferroelectric and photoluminescent properties in perovskites. *Photoluminescence: Applications, Types and Efficacy*, pages 119–161, 01 2012.

[10] Jessica Hermet. Theoretical study of protonic conduction in gd-doped baceo3 : an electrolyte for fuel cell. 10 2013.

[11] Eric Langenberg, Laura Maurel, Guillermo Antorrena, Pedro Algarabel, César Magén, and Jose Pardo. Relaxation mechanisms and strain-controlled oxygen vacancies in epitaxial srmno 3 films. *ACS Omega*, XXXX, 05 2021.

[12] Jun Hee Lee and Karin M. Rabe. Epitaxial-strain-induced multiferroicity in srmno$_3$ from first principles. *Phys. Rev. Lett.*, 104:207204, May 2010.

[13] Alexander Edström and Claude Ederer. Prediction of a giant magnetoelectric cross-caloric effect around a tetracritical point in multiferroic srmno$_3$. *Phys. Rev. Lett.*, 124:167201, Apr 2020.

[14] L. Wu, S. Nikitin, Matthias Frontzek, Alexander Kolesnikov, G. Ehlers, Mark Lumsden, K. Shaykhutdinov, Er-Jia Guo, A. Savici, Zheng Gai, A. Sefat, and Andrey Podlesnyak. Magnetic ground state of the ising-like antiferromagnet dysco$_3$. *Physical Review B*, 96, 092017.

[15] Shuji Hasegawa. *Reflection High-Energy Electron Diffraction*, pages 1–14. John Wiley Sons, Ltd, 2012.

[16] Y Kainuma. The theory of kikuchi patterns. *Acta Crystallographica*, 8(5):247–257, 1955.

[17] Carsten Becher, Laura Maurel, Ulrich Aschauer, Martin Lilienblum, César Magén, Dennis Meier, Eric Langenberg, Morgan Trassin, Javier Blasco, Ingo P Krug, et al. Strain-induced coupling of electrical polarization and structural defects in srmno3 films. *Nature nanotechnology*, 10(8):661–665, 2015.

[18] J. Kleibeuker, Bouwe Kuiper, S. Harkema, Dave Blank, Gertjan Koster, Guus Rijnders, P. Tinnemans, E. Vlieg, P. Rossen, G. Portale, Jayakanth Ravichandran, and R. Ramesh. Structure of singly terminated dysco3 (110) surfaces. *Physical Review B - PHYS REV B*, 85, 04 2012.